



저작자표시-비영리-변경금지 2.0 대한민국

이용자는 아래의 조건을 따르는 경우에 한하여 자유롭게

- 이 저작물을 복제, 배포, 전송, 전시, 공연 및 방송할 수 있습니다.

다음과 같은 조건을 따라야 합니다:



저작자표시. 귀하는 원저작자를 표시하여야 합니다.



비영리. 귀하는 이 저작물을 영리 목적으로 이용할 수 없습니다.



변경금지. 귀하는 이 저작물을 개작, 변형 또는 가공할 수 없습니다.

- 귀하는, 이 저작물의 재이용이나 배포의 경우, 이 저작물에 적용된 이용허락조건을 명확하게 나타내어야 합니다.
- 저작권자로부터 별도의 허가를 받으면 이러한 조건들은 적용되지 않습니다.

저작권법에 따른 이용자의 권리는 위의 내용에 의하여 영향을 받지 않습니다.

이것은 [이용허락규약\(Legal Code\)](#)을 이해하기 쉽게 요약한 것입니다.

[Disclaimer](#)

Master's Thesis of Science

**A Semi-Empirical Threshold Model for Oil Spill
Detection by Analyzing Microwave Backscattering of
Ocean Surface**

유류오염 탐지를 위한 해양표면 마이크로파
후방산란 분석기반의 준경험적 임계모델

August 2023

Graduate School of Earth and Environmental Sciences

Seoul National University

Soyeon Park

**A Semi-Empirical Threshold Model for Oil
Spill Detection by Analyzing Microwave
Backscattering of Ocean Surface**

유류오염 탐지를 위한 해양표면 마이크로파
후방산란 분석기반의 준경험적 임계모델

지도 교수 김 덕 진

이 논문을 이학석사 학위논문으로 제출함
2023 년 5 월

서울대학교 대학원
자연과학대학 지구환경과학부
박 소 연

박소연의 이학석사 학위논문을 인준함
2023 년 7 월

위 원 장 조 양 기 (인)

부위원장 김 덕 진 (인)

위 원 박 상 은 (인)

Abstract

In an automatic oil spill monitoring system that utilizes SAR satellites, the dark spot detection step, which is responsible for the segmentation of potential oil spills, is undeniably significant. As the initial stage of automatic oil spill detection, this process is typically the most time-consuming and substantially influences the system performance. Considering the vast expanses of ocean that require thorough surveillance, it is crucial to have an efficient method that accurately identifies oil spill candidates at this critical early stage. In this study, a semi-empirical model was carefully proposed, grounded in a comprehensive analysis of the physical characteristics governing the interaction between electromagnetic waves and the sea surface, as well as oil spill observation data from SAR. This model utilizes wind speed, relative wind direction, and incidence angle as independent variables to calculate the threshold radar backscatter coefficient, to differentiate oil spill candidates from the ocean. To determine the parameters of the proposed model, large oil spill observational data was collected from the Sentinel-1 satellite, and the corresponding wind field data was derived from the ECMWF ERA5 reanalysis data.

When compared to widely used dark spot detection methods such as the Otsu, Bradley, and active contour methods, the proposed model demonstrated outstanding performance. The model achieved an average F1 score of 0.7948 on the evaluation dataset, while the aforementioned methods showed 0.3315, 0.6400, and 0.5191, respectively. The proposed model exhibited distinguished accuracy

with a straightforward implementation process, balancing effectiveness with simplicity, which makes it particularly suitable for real-time oil spill detection where efficiency is paramount. A notable feature of the proposed model is its ability to compute threshold at the pixel-level, unlike conventional patch-level methods that require iterative processes to detect oil spill candidates of varying sizes. This allows the model to identify oil spills in a single operation regardless of their sizes. While the proposed model is flexible in using diverse wind input sources such as buoys, scatterometers, or geophysical model functions, it is crucial to note that its performance depends on the accuracy of the wind field information, specifically, how well it reflects the wind conditions at the exact SAR acquisition time.

In conclusion, this study has thoroughly investigated the behavior of the radar backscatter coefficient under both slick-free and slick-covered sea surfaces, leading to the development of a semi-empirical model that can enhance the efficiency of oil spill monitoring systems. The practical implications of the model extend beyond improving system performance; it can be used to create balanced deep-learning datasets by selectively choosing patches with dark spots. Moreover, the physically-grounded nature of the model enables advanced future research, such as distinguishing types of oil or estimating slick thickness.

Keywords: SAR, Oil spill, Microwave backscattering, Semi-empirical model, Segmentation

Student Number: 2021-22292

Table of Contents

Chapter 1. Introduction.....	1
1.1 Research Background.....	1
1.2 Literature Review.....	4
1.3 Research Objective.....	9
Chapter 2. Microwave Backscattering Properties from the Sea Surface.....	11
2.1 Microwave backscattering from the Slick-Free Ocean Surface	11
2.1.1 Radar Scattering Model.....	11
2.1.2 Geophysical Model Function	13
2.2 Microwave backscattering from the Slick-Covered Ocean Surface.....	18
2.2.1 The Action Balance Equation.....	18
2.2.2 The Damping Ratio	27
Chapter 3. Development and Validation of the Semi-Empirical Model	29
3.1 Formulation of the Theoretical Framework for the Semi-Empirical Model	29
3.2 Data Acquisition.....	34
3.2.1 Acquisition of SAR Image Data.....	34
3.2.2 Acquisition of Wind Field Data	40

3.3	Parameter Determination of the Semi-Empirical Model.....	44
Chapter 4.	Performance Evaluation of the Semi-Empirical Model....	47
4.1	Experimental Design.....	47
4.2	Performance Evaluation with Other Methods.....	51
4.3	Performance Evaluation for Different Wind Conditions and Regions.....	60
Chapter 5.	Application of the Semi-Empirical Model	69
Chapter 6.	Conclusion.....	72
Bibliography	75
Abstract in Korean	82

List of figures

Fig. 2.1. SAR backscatter coefficient distribution as estimated by the CMOD5.N model.	17
Fig. 2.2. Relative viscous damping coefficient $y(k)$ as a function of wavenumber. The black vertical lines represent the wavenumber k_M corresponding to the maximum value of $y(k)$	26
Fig. 2.3. Radar backscatter coefficient for slick-free and slick-covered area by incidence angle.	28
Fig. 3.1. (a) Visualization of the wind energy-driven dispersion of oceanic waves across the sea surface. (b) Illustration of the wave component discernible by the satellite.	33
Fig. 3.2. The spatial distribution of the collected Sentinel-1 SAR images containing oil spills from May 2015 to September 2022.	37
Fig. 3.3. Flowchart of the data processing methodology.....	38
Fig. 3.4. (Left) A full Sentinel-1 SAR image containing oil slicks acquired on October 4, 2014. (Right) The oil pollution patch subtracted from the full SAR image.....	39
Fig. 3.5. ECMWF ERA5 reanalysis of wind speed at 10 meters on October 4, 2014.....	43
Fig. 3.6. The scatter plot represents the observational data, and the line plot shows the model results with the optimized coefficient.....	46

Fig. 4.1. Violin plot illustrating the distribution of the F1 score. Red bars indicate the mean F1 score.58

Fig. 4.2. Comparative visualization of the optimal results for various segmentation methods. Each row represents the best-performing case for a given method.....59

Fig. 4.3. Comparative visualization of the optimal results for various segmentation methods. Each row represents the worst-performing case for a given method.....59

Fig. 4.4. F1 score distribution of each model by wind speed.....62

Fig. 4.5. The violin plot of the semi-empirical model F1 score for each wind speed bin.....63

Fig. 4.6. Points where the F1 score is higher than 0.9 are represented on the wind speed standard deviation map.....66

Fig. 4.7. Points where the F1 score is lower than 0.7 are represented on the wind speed standard deviation map.....67

Fig. 4.8. Time-series analysis for wind speed at two regions.....68

Fig. 5.1. Comparison of results between model input wind dataset.....71

List of Tables

Table 2.1. The coefficients of the CMOD5.N model	16
Table 2.2. Viscoelastic properties and kinematic viscosity of the mineral oils	25
Table 3.1. Product characteristics of Sentinel-1 IW GRD mode.....	36
Table 3.2. Product characteristics of ECMWF ERA5 reanalysis data	42
Table 3.3. The optimized parameters and their corresponding standard errors	45
Table 4.1. Parameters required to tune the different methods of detecting dark spots.....	50
Table 4.2. Detailed evaluation of the dark spot detection methods.....	57
Table 4.3. Standard deviation and skewness for each dark spot detection method.....	58

Chapter 1. Introduction

1.1 Research Background

Marine oil pollution poses a significant threat to the environment, and it is imperative to identify the precise discharge area through regular ocean surveillance in order to minimize its effects. Synthetic Aperture Radar (SAR) is an active sensor that transmits electromagnetic waves and measures the backscattered signal from targets, making it capable of image acquisition regardless of sunlight and weather conditions. Numerous studies have demonstrated the effectiveness of SAR in observing oil spills (Gade and Alpers, 1999; Del Frate et al., 2000; Solberg et al., 2007; Kim et al., 2010; Marghany, 2014; Xu et al., 2014; Singha et al., 2016). In ocean radar imaging, the intensity values in SAR scenes represent the power of the backscattered radar signal from the sea surface. When the sea surface is covered with an oil slick, the slick attenuates the ocean surface wave, having a darker brightness value than the slick-free surroundings.

However, dark areas do not always result from anthropogenic mineral oil spills. Non-oil features that appear similar to oil spills in SAR imagery are referred to as oil spill look-alikes and these can originate from various sources such as (i) natural surface films formed by plankton or fish, (ii) areas with low winds that smooth out the sea surface, (iii) cold upwelling water which changes the stability of the air-sea interface, (iv) divergent flow regimes, (v) dry-fallen sands during ebb

tide, (vi) turbulent waver as encountered in ship wakes, (vii) turbulence caused by rain drops which dampen the short waves, (viii) grease or frozen sea ice, or (ix) sewage plants from the land (Alpers et al., 2017). The most common causes are natural surface films by marine organisms, typically referred to as biogenic slicks and low wind areas. Considerable efforts have been made to develop automatic systems that can effectively differentiate anthropogenic mineral oil spills from various types of oil spill look-alikes.

The automatic oil spill detection method typically involves three steps: dark spot detection, dark spot feature extraction, and dark spot classification (Brekke and Solberg, 2005). The initial step involves the detection or segmentation process of dark spots, which aims to distinguish oil spill candidates from the background. In subsequent steps, feature extraction processes are employed to identify unique characteristics or statistical parameters of the detected dark spots. These characteristics can be used to classify dark spots as oil spills or oil spill look-alikes. Following the feature extraction, a classifier is used to determine whether the potential oil spills identified during the dark spot detection step are anthropogenic mineral oil spills or look-alikes.

The accurate detection of dark spots is crucial as it impacts the overall performance of the oil spill identification process. Failure to detect an oil slick during the dark spot segmentation step can result in incorrect classification of the oil spill (Brekke and Solberg, 2005). Furthermore, detecting dark spots has historically been the most time-consuming step of the three (Shu et al., 2010). Therefore, an optimal approach for dark-spot detection is imperative to the

successful development of automated oil-spill detection systems, as it enhances their efficiency and effectiveness.

1.2 Literature Review

A variety of advanced methods have been employed to detect dark spots, including (i) region-based methods, (ii) histogram-based methods, (iii) adaptive threshold methods, (iv) deformable model methods, (v) object-oriented segmentation methods, and (vi) neural networks. In most cases, a combination of multiple methods is utilized for better oil spill segmentation.

When dealing with SAR images, which inherently exhibit speckle noise, region-based segmentation is often employed. This method is widely used due to its effectiveness in distinguishing dark areas, even within noisy images. In this method, adjacent pixels with similar intensities are grouped into unique regions. Del Frate et al. (2000) used a combination of histogram-based analysis and region-based segmentation, while Mihoub and Hassini (2014) employed a region-merging method iteratively to detect multiple sizes of oil spills.

The histogram-based method has been used for a long time since its introduction by Otsu (1979). Liu et al. (2010) combined the Otsu and Max-entropy methods, while Yu et al. (2017) proposed an adaptive mechanism based on the Otsu method to extract possible oil spills. To increase the segmentation performance, a spatial density threshold algorithm was proposed in (Shu et al., 2010). The Otsu method was used initially for intensity segmentation, then spatial density segmentation was applied to distinguish pixels with high threshold density.

The adaptive threshold algorithm calculates threshold values dynamically for small window sizes under the assumption that local regions of the image will have

more uniform illumination. As the SAR has different brightness values depending on the incidence angle, the adaptive threshold was effective in many approaches. Solberg et al. (1999) determined the threshold as k dB below the mean value of the moving window. Keramitsoglou et al. (2006) combined the adaptive threshold method with a fixed window size of 41 by 41, and the k -distance metric to merge smaller groups into bigger ones. Solberg et al. (2007) enhanced the adaptive thresholding method by categorizing the roughness of the surrounding sea into six bins to set threshold values more effectively. Zeng and Wang (2020) developed an iterative adaptive thresholding algorithm to compensate for SAR image brightness variation.

Deformable models such as Active Contour Model (ACM) and level-set methods were widely used in medical image segmentation, demonstrating promising results. By minimizing the energy functionals based on both image data and characteristic features, it is possible to identify or segment objects (Padmasini et al., 2018). As this approach generally performs well over weak boundaries, the method was used to detect possible oil spills. Karantzas and Argialas (2008) employed the Mumford and Shah (MS) curve evolution algorithm. Xia et al. (2015) exploited a multiscale active contour model based on the nonlocal processing principle. The combination of the iterative Otsu method and the level-set method was proposed in (Mdakane and Kleynhans, 2017), and (F. Chen et al., 2018) formulated own energy functionals for segmentation.

Considerable work has been performed to detect dark spots of different sizes. The object-oriented method is commonly used with an iterative process to detect

dark patches of various sizes. In (Karathanassi et al., 2006) and (Topouzelis and Psyllos, 2012) object-oriented methodology was used, which utilizes a bottom-up region-merging segmentation algorithm based on two empirical formulas in two different scales: detailed and broad. Konik and Bradtke (2016) utilized multilevel hierarchical segmentation from the object-oriented methodology. The iterative region-merging may start from the pixel level or an existing image object distinguished as a lower level of hierarchy.

Dark spot detection using neural networks has been widely employed. Initially, fully connected feedforward networks with simple structures were used to detect dark spots, as done by Topouzelis et al. (2007) and Singha et al. (2013). Some of the neural network methods proposed in (Krestenitis et al., 2019; Bianchi et al., 2020; Shaban et al., 2021) combined dark spot detection with other steps that enable the neural network model to learn features from the oil spill. Krestenitis et al. (2019) used SAR intensity images containing segmentation masks with five classes as training data: oil spills, look-alikes, ships, land, and sea surface. With the training data, six different semantic segmentation models were compared, and DeepLabv3+ demonstrated the best overall performance. Bianchi et al. (2020) used a U-net based semantic segmentation model with training data classified into two classes: oil and non-oil. Shaban et al. (2021) used two types of neural networks. The SAR image patches with more than 1% oil spill instances were prescreened with the CNN model, and the five-stage U-net architecture was used to segment the oil spill area.

While each of the aforementioned methods has its own benefits, there are also some limitations associated with them. First, the performance is highly dependent on tuning parameters such as window size, sensitivity, and stopping criteria (i, iii, iv, v, vi). Additionally, the model performance significantly drops when outlier pixels are not properly removed, such as vessels or large ocean buoys, are present on the ocean surface (i, ii, iii, v). Lastly, some methods are limited in their ability to detect oil spills of different sizes (i, ii, iii), and iterative processes are typically used to address this issue, which can be computationally inefficient (iv, v).

Therefore, in order to enhance the capability to distinguish oil spills from look-alikes and to reduce the number of false alarms, the need to take into account the local wind field was recognized. Since the local surface wind condition greatly influences the surface capillary waves, several researchers have attempted to utilize wind information in oil spill detection. For instance, Espedal and Wahl (1999) detected oil spill patches by identifying areas that are 2dB darker than their surroundings and if the wind speed at the time or within recent history is greater than 7m/sec, the patch was classified as an oil spill. Solberg et al. (2007) proposed variable threshold values for dark spot detection, which were dependent on wind speed and categorized into six distinct levels. The wind field data was employed as an additional input to the neural network as well. Salvatori et al. (2003) used wind vectors estimated from SAR images as an additional input to a neural network model to improve the performance of oil spill detection. Similarly, in (Chen and Wang, 2022), wind vector data estimated from SAR images was also used as one of the inputs of the designed Attention U-net model.

While the introduction of wind field data to detect oil spills was effective in the research above, only a specific range of wind has been used as a threshold for oil slick detection, or the SAR-induced wind information was utilized which may be inaccurate where objects exist on the surface. Also, only the interaction between wind and sea surface was considered and the physical mechanisms between microwave and sea surface, particularly in relation to oil slicks, are still not fully considered. Therefore, it is essential to understand the relationship between radar detection and various wind conditions, which lead to the development of more reliable and accurate methods for detecting oil slicks.

1.3 Research Objective

Through the previous section, various approaches to identify oil spill candidates and the limitations of those methods were outlined. The objective of this research is to enhance an understanding of the radar backscattering coefficient values for various ocean surfaces. Building upon this theoretical background, a semi-empirical threshold model for dark spot detection is aimed to be developed, incorporating actual observational data from oil spills to represent real-world scenarios. Consequently, the proposed dark spot detection model could provide a more efficient and effective method for oil spill detection. In summary, the main contributions of this research are as follows:

- This study proposes a physically reasonable model by considering the SAR ocean imaging process. The model provides interpretable results and has better control over its behavior, potentially facilitating advanced oil spill detection methods such as distinguishing oil types or estimating slick thickness.
- The proposed model helps in efficient oil spill detection by detecting dark spots with a high possibility of oil spill. It effectively screens out low-wind areas, which are commonly known to be the most frequent and problematic look-alikes with biogenic slicks.
- The proposed model has a high level of accuracy as it remains insensitive to outliers such as vessels or large ocean buoys.

- The model does not require any tuning parameters for oil spill detection. In this regard, the proposed model can assist in oil spill training dataset construction for deep-learning.
- Utilizing the semi-empirical model, it is possible to construct a computationally efficient oil spill detection system. Given that the model works on a pixel-by-pixel basis rather than using a window-based method, it circumvents the need for iterative processes in detecting oil spills of any size.

The remainder of the thesis is organized as follows. Chapter 2 examines microwave backscattering characteristics from both slick-free and slick-covered surfaces. Chapter 3 details the development and validation of the semi-empirical model, starting with the theoretical framework, progressing to data acquisition, and culminating in parameter determination and validation. Chapter 4 provides an evaluation of the semi-empirical model in comparison with other methods for segmenting oil spills. Lastly, Chapter 5 demonstrates the application of the model in oil spill detection.

Chapter 2. Microwave Backscattering Properties from the Sea Surface

Microwave backscattering from the sea surface is governed by complex physical factors, and the characteristics of microwave backscattering are examined for the slick-free and slick-covered surfaces in the following chapter.

2.1 Microwave backscattering from the Slick-Free Ocean Surface

2.1.1 Radar Scattering Model

The radar backscatter coefficient can be explained differently depending on the viewing geometry of SAR. At low incidence angles, the radar backscatter is dominated by specular reflection, while at intermediate angles, Bragg scattering is the dominant mechanism (Alpers et al., 2017). The Bragg scattering model explains that the backscatter coefficients are determined by ocean waves with the Bragg wavenumber of k_B , which is in resonance condition with radar wavenumber k_e (Franceschetti et al., 2002). This resonance condition is called the Bragg resonance condition,

$$k_B = 2k_e \sin\theta \quad (2.1)$$

where θ is the incidence angle of the SAR.

When SAR utilizes microwave wavelength, water waves with short gravity capillary wavelength range that travel parallel to the line of sight make a significant contribution to the radar backscatter coefficient (Valenzuela, 1978). In the first-order approximation, when the capillary wave is not tilted with respect to a horizontal reference plane, the radar backscatter coefficient (σ_0) of the ocean is given as below (Wright, 1968).

$$\sigma_0 = 8\pi k_e^4 \cos^4(\theta) |b_p(\theta)|^2 [\Psi(k_B) + \Psi(-k_B)] \quad (2.2)$$

Here, the complex scattering coefficient b has a different value for polarization p . The approximation value of the complex scattering coefficient for the VV polarization can be written as

$$b_{VV} = \frac{\epsilon^2(1 + \sin^2\theta)}{(\epsilon \cos\theta + \sqrt{\epsilon})^2} \quad (2.3)$$

where ϵ denotes the relative dielectric constant of seawater. The term Ψ represents the wave height spectrum, which of its integral is defined as the expectation of the square of the surface elevation ζ (mean surface elevation) (Romeiser et al., 1997)

$$\iint \Psi(k) d^2 k = \langle \zeta^2 \rangle \quad (2.4)$$

To obtain a more accurate representation of the actual sea surface, more complex theories have been proposed that take into account the geometric variations of surface slopes. These theories consider the impact of the tilt of

capillary waves at the Bragg resonance condition due to longer waves and are commonly referred to as the tilted Bragg scattering model, the composite-surface scattering model, or the two-scale Bragg scattering model. When dealing with slightly tilted Bragg scattering, the backscatter coefficient value for the VV polarization can be represented as (Valenzuela, 1978)

$$\sigma_{0VV} = 8\pi k_e^4 \theta_e [\Psi(k_B) + \Psi(-k_B)] \cdot \left| \left(\frac{\sin(\theta - s_p) \cos(s_n)}{\sin(\theta_e)} \right)^2 b_{VV}(\theta_e) + \left(\frac{\sin(s_n)}{\sin(\theta_e)} \right)^2 b_{HH}(\theta_e) \right|^2 \quad (2.5)$$

where s_p is slope parallel to the radar look direction and s_n denotes slope normal to the radar look direction. The effective local incidence angle θ_e is as follows.

$$\theta_e = \cos^{-1}[\cos(\theta - s_p) \cos(s_n)] \quad (2.6)$$

The two-scale Bragg scattering theory describes the SAR backscatter coefficient of a tilted facet with respect to a constant unit area in a horizontal reference plane.

2.1.2 Geophysical Model Function

With the use of a transmitting wave with a wavelength in the centimeter range, the ocean surface waves of the capillary range are detected according to the Bragg scattering theory. These waves are influenced by the local surface stress, which is primarily determined by the local surface wind condition. The physical mechanisms responsible for the generation of capillary waves by the local surface stress and the interaction of electromagnetic waves with the sea surface have been studied extensively over several decades. However, due to the limited range of

applicability of theory-based models, empirical approaches have been proposed to establish the relationship between wind and backscatter for practical applications (Hersbach, 2003). Empirical model functions which are called Geophysical Model Functions (GMFs) were presented through a large collocation study that observed radar backscatter from aircraft and spaceborne platforms along with in situ ocean buoy and Numerical Weather Prediction (NWP) model data (Hersbach, 2008).

A SAR-based sea surface wind retrieval algorithm was proposed across different wavelengths such as X-band (Li and Lehner, 2013; Nirchio and Venafrà, 2013) and L-band (Isoguchi and Shimada, 2009). The C-band model CMOD is widely used, with various versions available including CMOD4 (Stoffelen and Anderson, 1997), CMOD_IFR2 (Quilfen et al., 1998), CMOD5 (Hersbach, 2003), CMOD5.N (Hersbach, 2008). The general form of the CMOD model is expressed as

$$\sigma_0(\theta, u, \phi) = B0(c_0, u, \theta)[1 + B1(c_1, u, \theta)\cos(\phi) + B2(c_2, u, \theta)\cos(2\phi)]^p \quad (2.7)$$

where ϕ is the angle between the wind direction and SAR azimuth look angle (both measured from the north). The c_i , θ , u , and p denote coefficients, incidence angle, wind speed, and parameter, respectively. The B_i terms are functions of the wind speed and incidence angle. The dominant term, $B0$, sets the speed scale for a given measurement. The upwind-crosswind asymmetry, $B2$, allows for the determination of wind direction, while $B1$ attributes resolve a remaining 180-degree ambiguity in wind direction.

The CMOD5.N model is an updated version of CMOD5 as it represents the C-band backscatter value as a function of the equivalent neutral ocean wind vector at a 10-meter height and incidence angle. The model takes the same form as Eq. (2.7), and the coefficients which are listed in Table 2.1 are calibrated using data from the ERS-2 satellite, ASCAT scatterometers, and European Centre for Medium-Range Weather Forecasts (ECMWF) reanalysis data. The distribution of the estimated SAR backscatter coefficient, determined using the CMOD5.N model, is shown in Fig. 2.1. In general, the radar backscatter coefficients derived from GMF algorithms are in agree with in-situ measurements and composite Bragg scattering theory (Hwang et al., 2010).

Table 2.1. The coefficients of the CMOD5.N model

Coefficients	Value	Coefficients	Value
c_1	-0.6878	c_{15}	0.0066
c_2	-0.7957	c_{16}	0.3222
c_3	0.3380	c_{17}	0.0120
c_4	-0.1728	c_{18}	22.700
c_5	0.0000	c_{19}	2.0813
c_6	0.0040	c_{20}	3.0000
c_7	0.1103	c_{21}	8.3659
c_8	0.0159	c_{22}	-3.3428
c_9	6.7329	c_{23}	1.3236
c_{10}	2.7713	c_{24}	6.2437
c_{11}	-2.2885	c_{25}	2.3893
c_{12}	0.4971	c_{26}	0.3249
c_{13}	-0.7250	c_{27}	4.1590
c_{14}	0.0450	c_{28}	1.6930

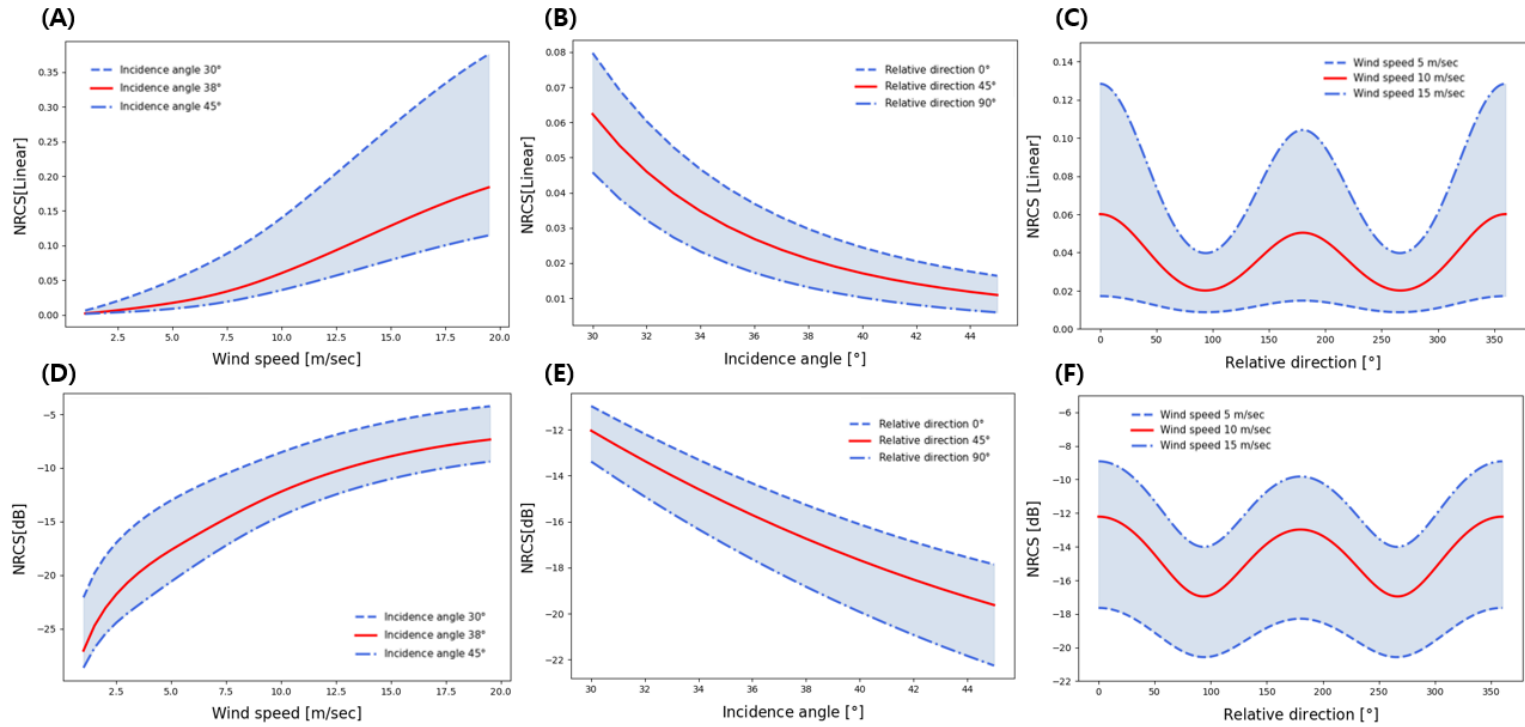


Fig. 2.1. SAR backscatter coefficient distribution as estimated by the CMOD5.N model.

2.2 Microwave backscattering from the Slick-Covered Ocean Surface

2.2.1 The Action Balance Equation

The presence of oil slicks on the ocean surface has a significant impact on the formation of ocean waves, causing a reduction in ocean surface height. The degree of attenuation varies depending on the type and amount of oil (Mitsuyasu and Honda, 1986). As a consequence of the weakened ocean waves, the electromagnetic return in the SAR system is also reduced, as stated in Eq. (2.2), (2.4), and (2.5). Therefore, a detailed assessment of how oil slick affects the ocean spectrum is essential for an accurate estimation of the SAR backscatter coefficient value in slick-covered areas.

The typical way of describing the sea state is using the action density spectrum denoted as N , which is also known as the spectral action density. This parameter is proportionate to the ocean wave height spectrum, represented as Ψ , and the phase velocity c_p .

$$N = c_p \cdot \Psi \quad (2.8)$$

The phase velocity c_p is defined as ω/k . ω represents the angular frequency of the ocean surface wave. For gravity-capillary waves, where the wave behavior is influenced by surface tension, the corresponding dispersion relation can be described as

$$\omega^2 = \left(gk + \frac{\sigma}{\rho} k^3 \right) \quad (2.9)$$

where g is the acceleration of gravity, k is the wavenumber of the ocean surface, σ is the water surface tension, and ρ is the density of water.

The spatial and temporal variations in wave spectral density N can be described with the source terms of energy input and output as (Elfouhaily et al., 1997)

$$\frac{dN}{dt} = \frac{\partial N}{\partial t} + c_g \nabla N = S_w - S_v + S_n - S_b \quad (2.10)$$

where c_g represents group velocity, which is defined as $\partial\omega/\partial k$. Using the deep-water approximations for the dispersion relation, it can be approximated as $c_g = g/2$. S_w , S_v , S_n , and S_b on the right-hand side are the source terms of the energy input and loss by wind, viscous dissipation, nonlinear wave-wave interaction, and wave breaking, respectively. Assuming a steady wind is blowing horizontally over the water surface, the action spectral density stays constant over time. In the case of short waves, such as gravity capillary waves, the gradient of N , which represents wave advection, can be assumed to be zero. Therefore, for the spectrally balanced case, Eq. (2.10) can be written as follows (Elfouhaily et al., 1997).

$$S_w - S_v + S_n - S_b = 0 \quad (2.11)$$

Depending on whether the ocean surface is slick-free or slick-covered, each source term has a different value. To examine the changes in source terms affected

by oil spills, slick-free is represented by a superscript of (f) and slick-covered by a superscript of (c).

The source term for wind input can be expressed as (Plant, 1982; Mitsuyasu and Honda, 1982).

$$S_w^{(f)} = \beta^{(f)} N^{(f)} = \left[0.04 (\cos \varphi) \left(\frac{u_*}{c_p} \right)^2 \omega \right] N^{(f)} \quad (2.12)$$

where $\beta^{(f)}$ represents the wind growth rate, describing the transfer of energy directly from wind to surface waves. The angle between the wind and wave direction is denoted by φ , and u_* is wind friction velocity which quantifies the transfer of momentum between the surface and the atmosphere. The friction velocity can be estimated from the 10-meter wind velocity, and in this study, the empirical formulas for the ocean (Yelland and Taylor, 1996) were used.

$$u_* = \sqrt{\frac{0.29u_{10}^2 + 3.1u_{10} + 7.7}{1000}}, \quad (u_{10} \leq 6 \text{ m/s}) \quad (2.13)$$

$$u_* = \sqrt{\frac{0.6u_{10}^2 + 0.07u_{10}}{1000}}, \quad (6 \leq u_{10} \leq 26 \text{ m/s}) \quad (2.14)$$

To describe energy input by the wind when the slick covers the ocean surface, a parameter m is introduced, which describes the reduction of the wind friction velocity by a surface film. Therefore, the wind input source term for the slick-covered area can be expressed as follows.

$$S_w^{(c)} = \beta^{(c)} N^{(c)} = \left[0.04 (\cos \varphi) \left(\frac{m \cdot u_*}{c_p} \right)^2 \omega \right] N^{(c)} \quad (2.15)$$

For the value m , 0.8 was used from the experiment by (Alpers and Hühnerfuss, 1989).

The source term for viscous dissipation in slick-free areas can be expressed as (Phillips, 1977)

$$S_v^{(f)} = 2\Delta^{(f)} c_g N^{(f)} = 2 \frac{4k^2 \eta \omega}{\rho(g + 3\tau k^2)} c_g N^{(f)} \quad (2.16)$$

where $\Delta^{(f)}$ is the damping coefficient of the gravity-capillary wave propagating on clean surfaces. η and τ are the dynamic viscosity of the water, and the ratio of the water surface tension and density, respectively.

In the case of a slick-covered sea surface, the Marangoni effect explains the attenuation by surface films made of surface-active materials (Alpers and Hühnerfuss, 1989). When gravity-capillary waves propagate on a water surface covered with a viscoelastic film, they give rise to local contractions and expansions of the surface film which in turn cause surface tension gradients. Marangoni waves can therefore be excited in this manner. Resonance occurs when the wavenumber of the surface wave at a given frequency matches that of the Marangoni wave, leading to maximum damping at this point. Therefore, the source term for viscous dissipation in slick-covered area is represented as

$$S_v^{(c)} = 2\Delta^{(c)} c_g N^{(c)} = 2 \cdot \gamma(k) \cdot \Delta^{(f)} c_g N^{(c)} \quad (2.17)$$

where $\Delta^{(c)}$ denotes the damping coefficients of the gravity-capillary wave propagating on slick-covered surfaces and can be calculated using $y(k)$, which is the relative viscous damping coefficient defined as $\Delta^{(c)}/\Delta^{(f)}$. Assuming mineral oil forms a monomolecular surface film over time, viscous damping by slicks can be described by its physical and chemical properties as follows (Alpers and Hühnerfuss, 1988).

$$y(k) = \frac{1 + X(\cos\theta - \sin\theta) + XY - Y\sin\theta}{1 + 2X(\cos\theta - \sin\theta) + 2X^2} \quad (2.18)$$

$$\text{with } X = \frac{|E|k^2}{(2\omega^3\eta\rho)^{0.5}}, \quad Y = \frac{|E|k}{4\eta\omega}$$

Here, the complex dilational modulus E is defined as the surface tension increment per unit fractional area change (dA/A) and can be expressed in the complex frequency plane (Callaghan et al., 1983).

$$E = \frac{A d\sigma}{dA} = -|E| \exp(i\theta) = |E| \cos\theta + i|E| \sin\theta \quad (2.19)$$

θ denotes the phase angle (viscous loss angle) between $\Delta\sigma$ and ΔA . The real component is surface dilatation elasticity, and the imaginary component is surface dilational viscosity. Table 2.2 presents the viscoelastic properties and kinematic viscosity at 15°C for four different types of oils (Wismann et al., 1993; Callaghan et al., 1983). The table also includes the maximum relative damping coefficient of Marangoni waves y_{max} , and the corresponding wavenumber at this maximum, k_M . The relative viscous damping coefficient across all wave numbers is depicted in Fig. 2.2. To calculate the relative damping coefficient, the following values were

used: water dynamic viscosity η at 0.001 Pa s , water density ρ at 1025 kg/m^3 , and acceleration of gravity g at 9.81 m/s^2 .

In the presence of an oil slick on the sea surface, the effect of damping caused by Marangoni waves is insufficient to fully account for the observed variations in the sea surface spectrum. While the Marangoni theory suggests that oil slicks only affect ocean waves with specific wavelengths, empirical evidence suggests that the entire spectrum is impacted by the presence of oil (Franceschetti et al., 2002). When winds transfer the energy to the ocean, the system reacts by distributing the energy throughout its spectrum by nonlinear wave-wave interactions. Thus, while the damping directly affects only short waves, longer waves are also influenced by the presence of oil. The strength of the wave-wave interaction mechanism is heavily influenced by wind intensity. The greater the wind intensity, the greater the energy-spreading effect. Therefore, nonlinear wave-wave interaction terms for slick-free are expressed as (Alpers and Hühnerfuss, 1989)

$$S_n^{(f)} = \alpha^{(f)}N^{(f)} = -q\beta^{(f)}N^{(f)} \quad (2.20)$$

where $\alpha^{(f)}$ is the nonlinear energy transfer rate for a clean sea surface. q is a dimensionless coefficient and is estimated as 1.15 by simulation (Franceschetti et al., 2002). Similarly, the source terms for slick-covered areas can be expressed as follows.

$$S_n^{(c)} = \alpha^{(c)}N^{(c)} \quad (2.21)$$

The $\alpha^{(c)}$ is the nonlinear energy transfer rate for slick-covered sea surface and can be represented below.

$$\alpha^{(c)} = \alpha^{(f)} + \delta\alpha \quad (2.22)$$

$$\text{with } \delta\alpha = \alpha_M \left(\frac{k}{k_M}\right)^{3/2} \left(\frac{u_*}{u_{*c}}\right)^2$$

The α_M represents the Marangoni damping rate and is presented as Eq. (2.23). u_{*c} is the critical frictional velocity which depends on the physicochemical properties of the surface film.

$$\alpha_M = 2c_g y(k_M) \Delta^{(f)}(k_M) = 2c_g \Delta_s(k_M) \quad (2.23)$$

At the center of the Marangoni attenuation, where the k is equal to the k_M , Marangoni damping is compensated by the nonlinear energy transfer at the wind stress of $u_* = u_{*c}$. Therefore, by assuming such a condition, Eq. (2.22) can be expressed as follows.

$$\alpha^{(c)} = \alpha^{(f)} + \alpha_M \quad (2.24)$$

Table 2.2. Viscoelastic properties and kinematic viscosity of the mineral oils

Substance	Viscosity (cSt)	 E (N/m)	θ (deg)	k_M (rad/m)	γ_{max}
Gas oil	5	0.0001	220	2663.1	1.259
IFO180	2000	0.00055	216	1089.3	2.011
North Sea crude oil	12.7	0.00165	-144	529.3	3.22
Middle East crude oil	16	0.00176	-158	565.7	3.689

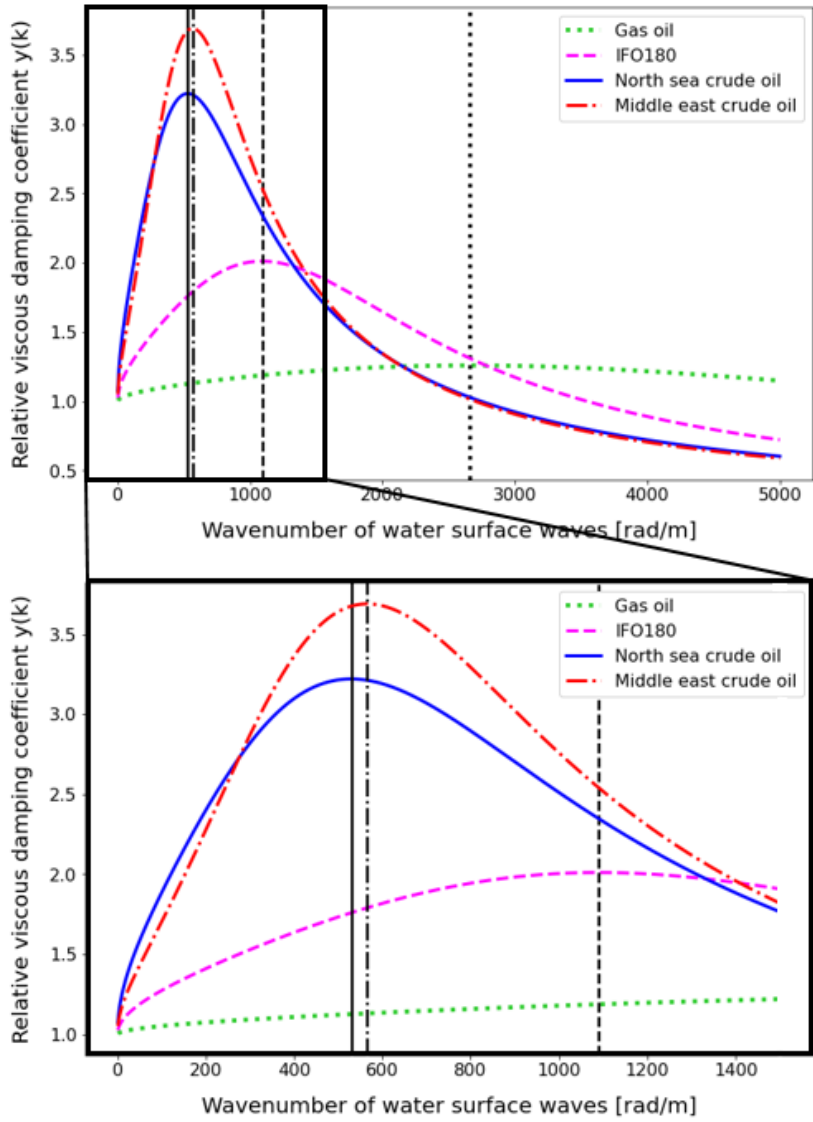


Fig. 2.2. Relative viscous damping coefficient $y(k)$ as a function of wavenumber.

The black vertical lines represent the wavenumber k_M corresponding to the maximum value of $y(k)$.

2.2.2 The Damping Ratio

The action balance equation was reviewed in the previous chapter to understand how oil spills affect the state of the sea. This chapter discusses how changes in sea state affect radar backscatter coefficients. The changes in the radar backscatter coefficient can be quantitatively assessed by employing the damping ratio, defined as a ratio of the σ_0 value for the presence and absence of a slick. The Bragg coefficient, denoting the residual part in Eq. (2.2) apart from the wave height spectrum, can be assumed to be the same for slick-free and slick-covered areas because the thickness of the surface film is small compared with the penetration depth of microwaves into the water (Gade et al., 1998). Additionally, according to Eq. (2.8), the wave height spectrum Ψ is proportional to the action density spectrum N . Hence, the damping ratio can be represented as follows.

$$\frac{\sigma_0^{(f)}}{\sigma_0^{(c)}} = \frac{\Psi^{(f)}(k_B)}{\Psi^{(c)}(k_B)} = \frac{N^{(f)}}{N^{(c)}} \quad (2.25)$$

In the first order, the source terms on the right-hand side of Eq. (2.10) are balanced for both slick-free and slick-covered cases (Alpers and Hühnerfuss, 1989). The sum of these source terms can be represented as follows.

$$(\beta^{(f)} - 2\Delta^{(f)}c_g + \alpha^{(f)}) \cdot N^{(f)} = (\beta^{(c)} - 2\Delta^{(c)}c_g + \alpha^{(c)}) \cdot N^{(c)} \quad (2.26)$$

$$\frac{N^{(f)}}{N^{(c)}} = \frac{(\beta^{(c)} - 2\Delta^{(c)}c_g + \alpha^{(c)})}{(\beta^{(f)} - 2\Delta^{(f)}c_g + \alpha^{(f)})} \quad (2.27)$$

Therefore, by combining Eq. (2.25) and Eq. (2.27), the damping ratio, which represents the ratio of the radar backscatter between the slick-free and slick-covered areas, can be derived as below.

$$\frac{\sigma_0^{(f)}}{\sigma_0^{(c)}} = \frac{\Psi^{(f)}(k_B)}{\Psi^{(c)}(k_B)} = \frac{N^{(f)}}{N^{(c)}} = \frac{(\beta^{(c)} - 2\Delta^{(c)}c_g + \alpha^{(c)})}{(\beta^{(f)} - 2\Delta^{(f)}c_g + \alpha^{(f)})} \quad (2.28)$$

As the radar backscatter value for the slick-free cases can be determined using the radar scattering model or the geophysical model function, the radar backscatter value for the slick-covered area can be estimated by multiplying the reciprocal of the damping ratio. In Fig. 2.3, the radar backscatter coefficient for slick-free areas was calculated using the CMOD5.N model, and the coefficient for slick-covered areas was then derived by applying the inverse of the damping ratio to the slick-free results.

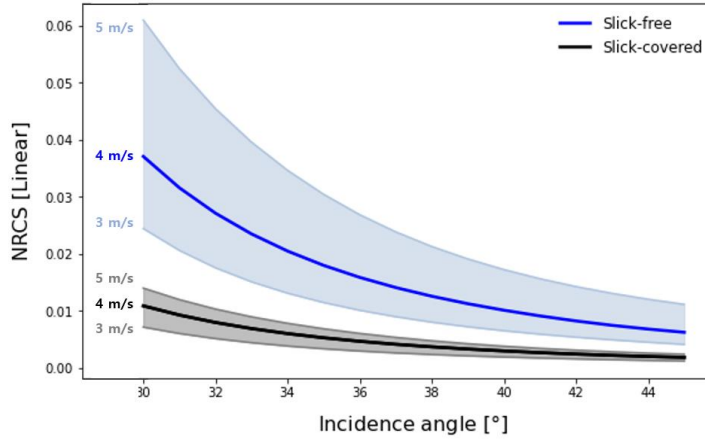


Fig. 2.3. Radar backscatter coefficient for slick-free and slick-covered area by incidence angle.

Chapter 3. Development and Validation of the Semi-Empirical Model

Based on the principles of ocean radar imaging physics, the goal of this study is to develop a model that effectively discriminates oil spill candidates from the ocean surface. A semi-empirical model, which combines physical principles with empirical observations, can provide a good balance between accuracy and simplicity. This chapter is dedicated to the exposition of the process involved in the formulation and subsequent validation of this semi-empirical model for oil spill detection.

3.1 Formulation of the Theoretical Framework for the Semi-Empirical Model

Considering the action balance equation and radar scattering model, the radar backscatter coefficient is dependent on many variables such as incidence angle, polarization, frequency of the radar, a relative dielectric constant of the surface, and surface roughness which is also dependent on wind speed, direction, ocean waves, and currents. Here, certain variables, including polarization and frequency of the radar are fixed as VV and C-band, respectively. Other variables, such as the relative dielectric constant, which has a small impact are not considered dependent variables in the semi-empirical model. Therefore, considering practical use and

maintaining the simplicity of the model, incidence angle, wind speed, and relative wind direction were chosen as dependent variables of the threshold model which is consistent with the dependent variables of GMFs.

To determine the boundary of the radar backscatter between the slick-free and slick-covered ocean with respect to wind speed, the wind growth rate β , in Eq. (2.12) and (2.15) from the action balance equation were reviewed. According to these equations, wind speed has a quadratic relationship with wave growth, expressed as u^2 . As the presence of slicks on the ocean surface affects the energy input by wind, coefficient m is incorporated into Eq. (2.15) to represent the reduction of wind friction velocity. Thus, the impact of wind speed on the threshold was theoretically determined as, Eq. (3.1) where d represents the coefficient that can be determined empirically.

$$(d \cdot u)^2 \tag{3.1}$$

To establish the theoretical relationship between wind direction and the threshold radar backscatter coefficient values, it is necessary to reflect the characteristics of the SAR satellite. In Eq. (2.12), the φ term represents the angle between wind and wave direction. It indicates how wind-induced waves spread out horizontally, with the range of angle from $-\pi/2$ to $\pi/2$ as depicted in Fig. 3.1 (a). When taking into account the heading direction of the SAR relative to the wind direction, as depicted in Fig. 3.1 (b), the wave components that the SAR identifies are those dispersed in the direction of the SAR heading angle from the original wind direction. In addition, assuming a simple Bragg scattering condition as

expressed in Eq. (2.2), the radar backscatter values for the directions φ and $\varphi + \pi$ are equivalent. Consequently, the wind direction dependence of the threshold value for the ocean slick is determined as

$$r \cdot |\cos(\varphi)| \quad (3.2)$$

where the coefficient r is derived from observational data.

In simple terms, the dependence of the radar backscatter on the incidence angle can be modeled as an inversion relationship, where the higher the incidence angle, the lower the corresponding σ_0 value. However, the relationship between incidence angle and radar backscatter coefficient is far more intricate. According to Eq. (2.1) and (2.2), σ_0 is a function of the incidence angle and multiple functions that are also dependent on the incidence angle as represented below.

$$\sigma_0 = 16\pi k_e^4 \cos^4(\theta) |b_p(\theta)|^2 \Psi(2k_e \sin\theta) \quad (3.3)$$

In this study, to maintain the simplicity of the model, the relationship between σ_0 and the incidence angle shown in Fig. 2.3 was adopted. Specifically, we set the threshold value to be the negative exponential of the incidence angle, as described in Eq. (3.4). The sensitivity of the exponential function is determined using observational data.

$$\theta^{-a} \quad (3.4)$$

Therefore, to summarize, the complete theoretical framework of the semi-empirical threshold model was constructed by integrating Eq. (3.1), (3.2), and (3.4).

$$\textit{Threshold } \sigma_0 = (d \cdot u)^2 + r \cdot |\cos(\varphi)| + \theta^{-a} + c \quad (3.5)$$

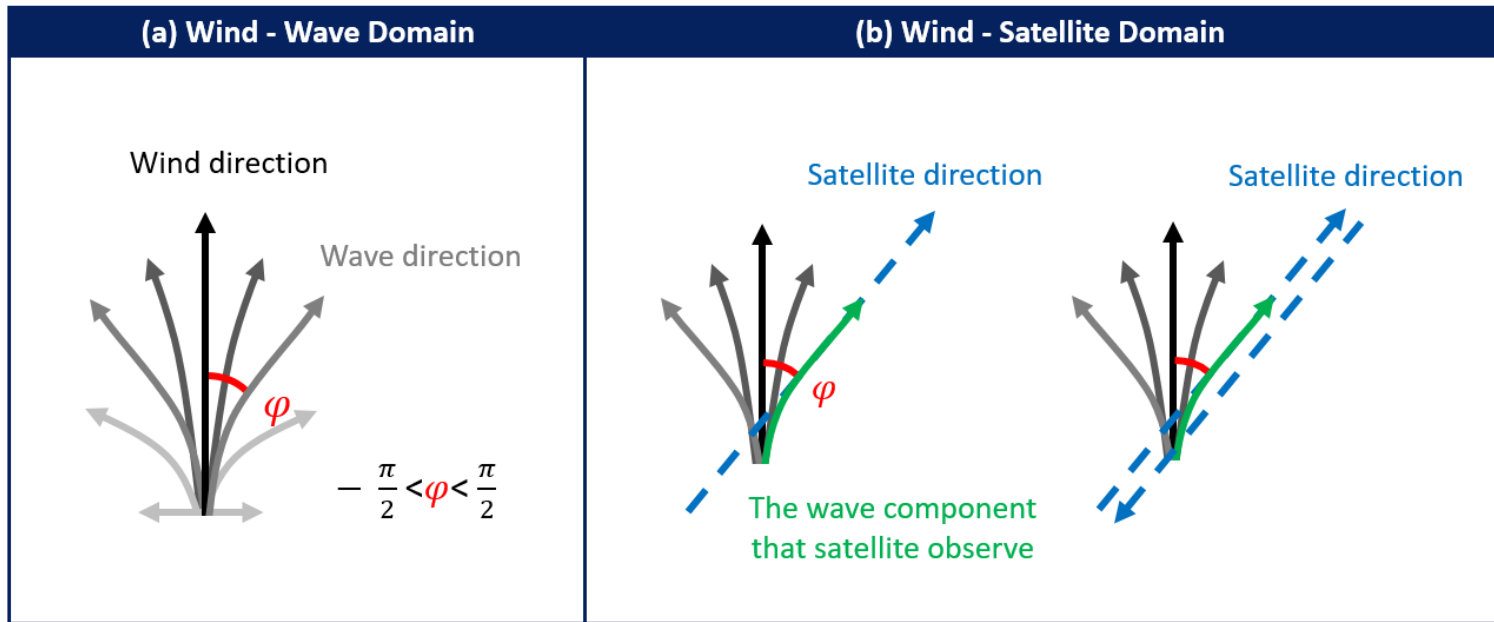


Fig. 3.1. (a) Visualization of the wind energy-driven dispersion of oceanic waves across the sea surface. (b) Illustration of the wave component discernible by the satellite.

3.2 Data Acquisition

3.2.1 Acquisition of SAR Image Data

In order to gather oil spill SAR imageries from worldwide, the Sentinel-1 SAR satellites from the European Space Agency (ESA) were utilized in this study. Since the shorter temporal resolution is more important in oil spill detection problems than higher spatial resolution, the Sentinel-1 SAR data which provides temporally dense data by making constellations with two satellites Sentinel-1A and Sentinel-1B could be useful. To get a wide swath and coverage with proper resolution the interferometric wide (IW) mode which has around 250 km of swath width and about 20 m by 23 m of spatial resolution (range and azimuth respectively) was used. Sentinel-1 Level 1 data are distributed under two product types which are Ground Range Detected (GRD) and Single Look Complex (SLC). Since the phase value is not used in this study, GRD data representing only the detected amplitude which is composed of square pixels with reduced speckle, due to the multi-look processing was used for this study. Details of Sentinel-1 IW GRD data were summarized in Table 3.1.

Basic information such as the time and location of oil pollution was obtained from publicly available data from the National Oceanic and Atmospheric Administration (NOAA) (<https://incidentnews.noaa.gov/browse/date/>) and International Tanker Owners Pollution Federation (ITOPF) (<https://www.itopf.org/>). Based on the obtained basic information, we collected 88 Sentinel-1 SAR images

from May 2015 to September 2022. The spatial distribution of the collected SAR images is depicted in Fig. 3.2. Before analysis, as shown in the flowchart of Fig. 3.3, SAR pre-processing is conducted in the following order: apply orbit file, radiometric calibration, speckle filtering, terrain correction, and land masking. Accurate satellite position and velocity information was obtained by updating the precise orbit of the satellite during the apply orbit file step, and radiometric calibration was performed to obtain a radar backscatter value, σ_0 from the digital numbers (DNs) of the SAR scenes. The Lee Sigma filter with a 7×7 window size was used for speckle filtering to reduce speckle noise, and the 3-second Shuttle Radar Topography Mission (STRM) Digital Elevation Model (DEM) was used for terrain correction and land masking. From the 88 pre-processed full SAR images, a total of 189 oil pollution patches each containing oil spilled area as a region of interest were produced from the SAR images as in Fig. 3.4. The Normalized Radar Cross Section (NRCS), incidence angle, and radar heading angle from the north for each pixel from the pre-processed SAR image were extracted. A visual interpretation was conducted to determine the true threshold σ_0 value for each patch and the values obtained were subsequently incorporated to calibrate the model.

Table 3.1. Product characteristics of Sentinel-1 IW GRD mode

Parameter	Sentinel-1 IW GRD
Center frequency	5.405 GHz
Polarization	VH, VV
Look direction	Right
Incidence angle range	20°- 46°
Pixel value	Magnitude detected
Coordinate system	Ground range
Bits per pixel	16
Number of Looks (range x azimuth)	5×1
Ground range coverage	251.8 km
Spatial resolution (range x azimuth)	IW1: 20.4 m × 22.5 m IW2: 20.3 m × 22.6 m IW3: 20.5 m × 22.6 m

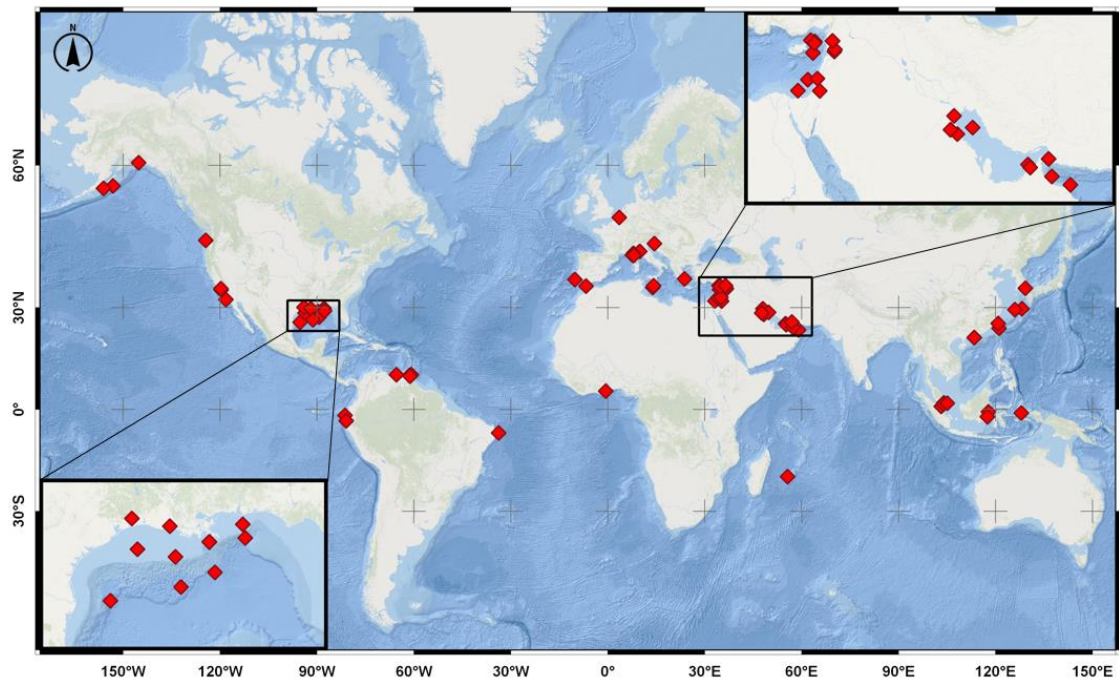


Fig. 3.2. The spatial distribution of the collected Sentinel-1 SAR images containing oil spills from May 2015 to September 2022.

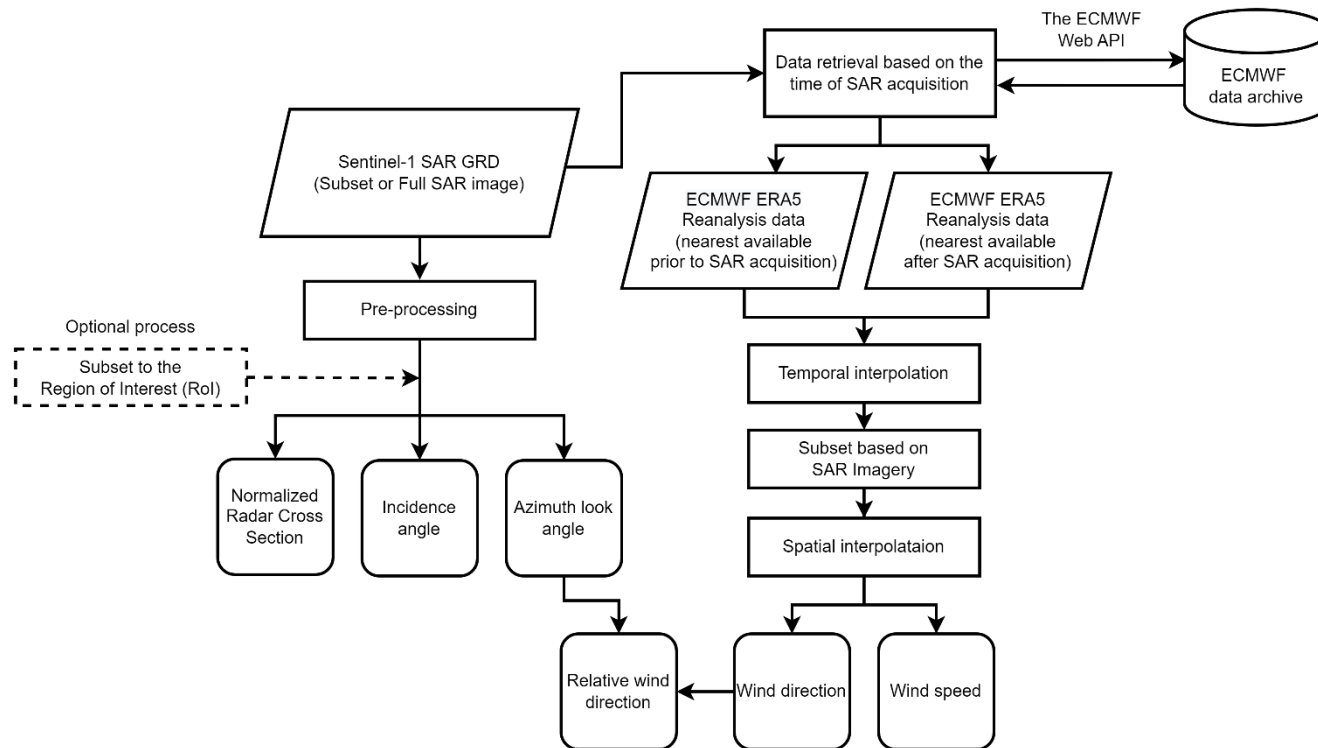


Fig. 3.3. Flowchart of the data processing methodology.

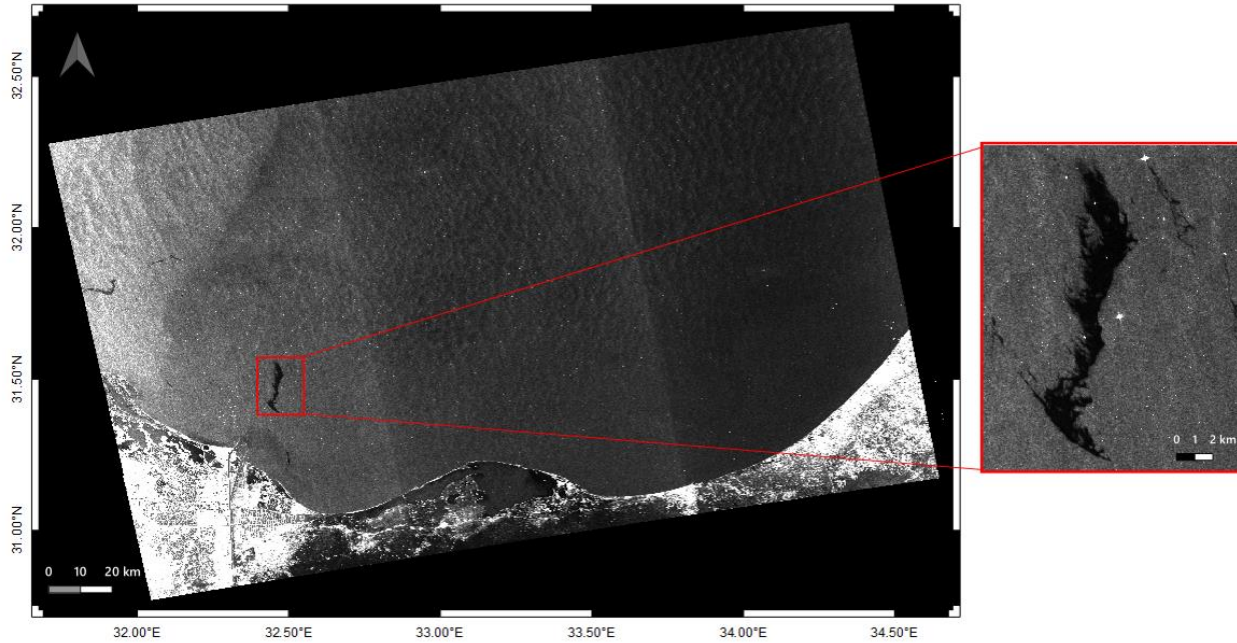


Fig. 3.4. (Left) A full Sentinel-1 SAR image containing oil slicks acquired on October 4, 2014. (Right) The oil pollution patch subtracted from the full SAR image.

3.2.2 Acquisition of Wind Field Data

A variety of methods exist for gathering information about ocean surface winds; these include the use of marine meteorological buoys, satellite scatterometers, SAR images, and reanalysis data. As each method has its unique strengths and weaknesses, selecting the most suitable one for global oil spill detection is crucial. While marine meteorological buoys provide in situ measurements, their coverage is limited to specific points and they cannot provide global coverage. On the other hand, while satellite scatterometer data allows for the regular monitoring of wind speed and direction across large areas, it is limited by its low spatial resolution and long revisit times. Wind data can also be derived from high-resolution SAR images using a GMF; however, SAR-extracted wind field data are subject to potential contamination from objects on the ocean surface. Reanalysis data, produced by integrating both observational data and numerical weather prediction models using data assimilation techniques, provides an accurate depiction of wind conditions.

Therefore, in this research, reanalysis data was employed to estimate the wind data around the oil spills, owing to its global completeness, temporal consistency, and quality-controlled nature. The ECMWF reanalysis data was selected as an external input for wind speed and direction. Specifically, the ERA5 model was chosen due to its higher resolution compared to other reanalysis models. The data was structured in regular latitude-longitude grids with a resolution of $0.28^\circ \times 0.28^\circ$ (31 km) and hourly temporal resolution and further details on ERA5 can be found

in Table 3.2. In this study, the hourly meridional and zonal 10 m wind components from the ERA-5 model, as illustrated in Fig. 3.5, were utilized to calculate the wind speed and direction over the oil spill area.

In order to align the resolution of the ERA5 data with that of the Sentinel-1 image, temporal and spatial interpolations were employed. Initially, two adjacent hourly reanalysis data were linearly interpolated to synchronize with the Sentinel-1 overpass time. Subsequently, the wind field was cropped to correspond to the same region as the SAR image and cubic spatial interpolation was applied to the region of interest. This procedure yielded wind speed and direction data that was consistent with the resolution of Sentinel-1.

By analyzing the SAR data, the values for σ_0 , incidence angle and SAR heading angle were obtained, and ECMWF reanalysis data were utilized to determine wind speed and direction. Subsequently, the relative wind direction, which is the wind direction relative to the satellite's flight direction, can be calculated from the SAR heading angle and the actual wind direction from the north. Thus, through the processing flow described in the flowchart, four output values were yielded: NRCS, incidence angle, relative wind direction, and wind speed, for each pixel.

Table 3.2. Product characteristics of ECMWF ERA5 reanalysis data

Parameter	ECMWF ERA5
Period available	1950 onwards
Horizontal resolution	0.28° x 0.28° (31 km)
Vertical resolution	137 levels
Temporal resolution	Hourly
Assimilation system	IFS* Cycle 41r2
Uncertainty estimates	From a 10-member EDA** at 63 km resolution

* Integrated Forecasting System (IFS)

** Ensemble of Data Assimilations (EDA)

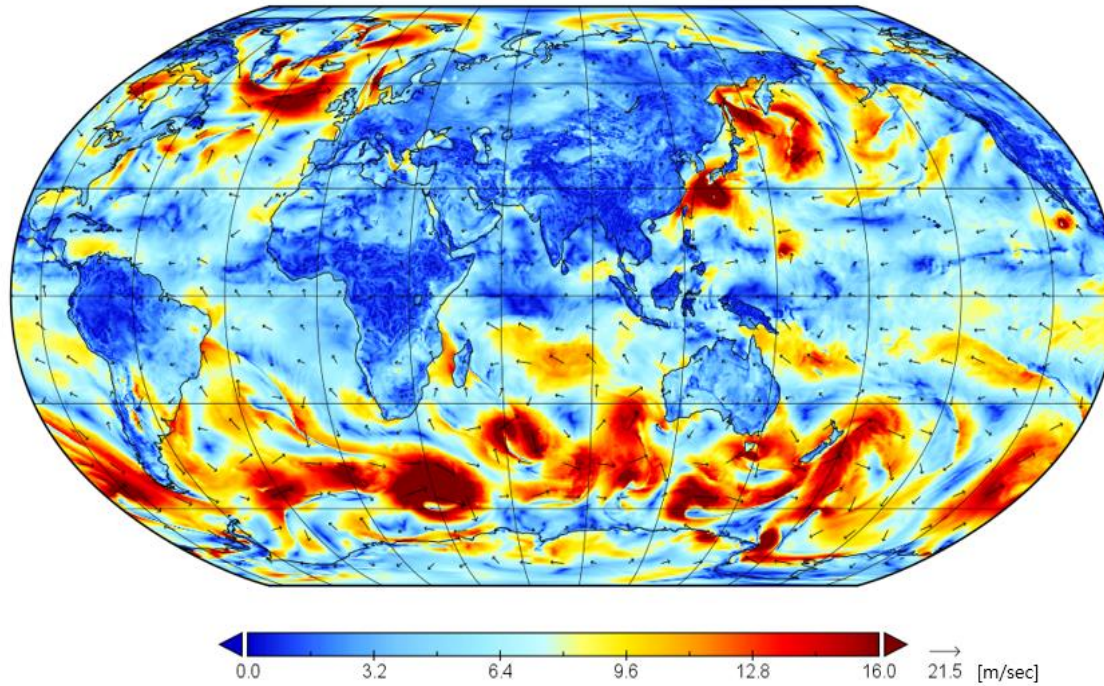


Fig. 3.5. ECMWF ERA5 reanalysis of wind speed at 10 meters on October 4, 2014.

3.3 Parameter Determination of the Semi-Empirical Model

Out of a total of 189 patches, each with pre-determined true threshold values, 151 patches (80% of the data) were randomly selected for parameter estimation, while the remaining 38 patches (20%) were reserved for validation. The model parameters in Eq. (3.5), specifically d, r, a and c were optimized by minimizing the sum of squared residuals. The calibrated parameters, along with their corresponding standard errors, are presented in Table 3.3. Specifically, the coefficient b was determined to be 9.4885×10^{-3} with a standard error of 9.6604×10^{-4} , the coefficient r was found to be 4.5919×10^{-4} with the standard error of 6.6402×10^{-4} , the coefficient a was determined to be 9.7717 with a standard error of 2.3393×10^{-2} , and the parameter c was found to be -2.3041×10^{-2} with a standard error of 2.5765×10^{-3} .

In evaluating the performance of the proposed model for estimating a threshold radar backscatter coefficient, a root mean square error (RMSE) of 0.0023 was achieved. This loss RMSE indicates a minor discrepancy between the model's estimation and the true radar backscatter coefficient values, signifying a reliable level of estimation accuracy. Additionally, an R-squared value of 0.6558 was obtained, suggesting the model's efficacy in capturing the underlying pattern within the data.

The model estimation results for the radar backscatter coefficient threshold are visualized in Fig. 3.6, compared with observational data. Estimated values are overlaid with the threshold values obtained from observations, and the figure depicts a close alignment between these two data sets.

Table 3.3. The optimized parameters and their corresponding standard errors

Parameter	Value	Standard error
<i>d</i>	9.4885×10^{-3}	9.6604×10^{-4}
<i>r</i>	4.5919×10^{-4}	6.6402×10^{-4}
<i>a</i>	9.7717	2.3393×10^{-2}
<i>c</i>	-2.3041×10^{-2}	2.5765×10^{-3}

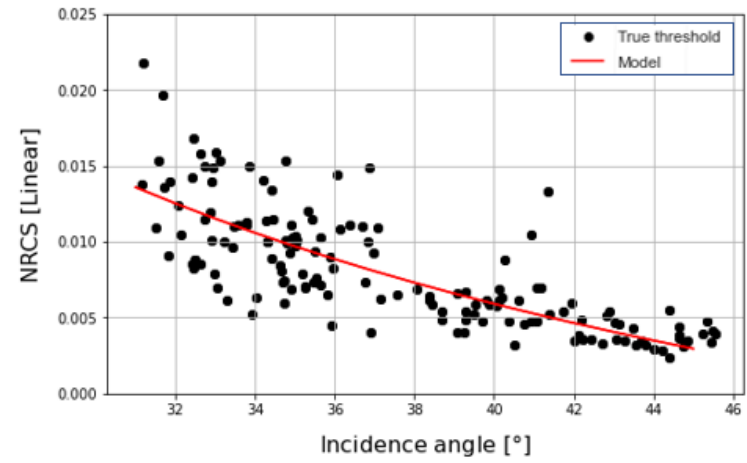
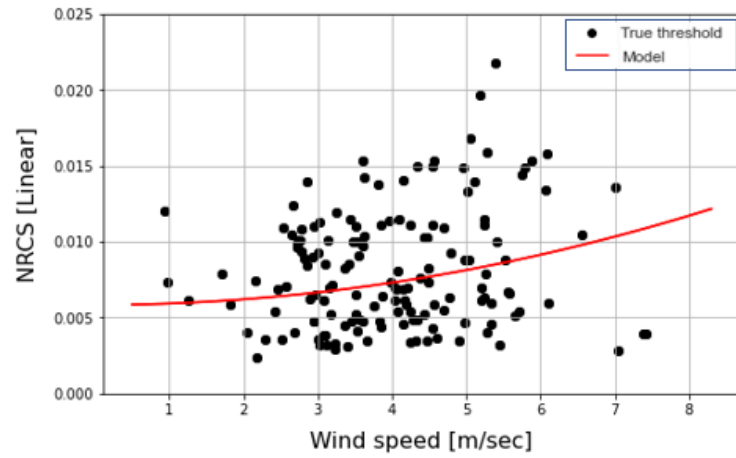


Fig. 3.6. The scatter plot represents the observational data, and the line plot shows the model results with the optimized coefficient.

Chapter 4. Performance Evaluation of the Semi-Empirical Model

4.1 Experimental Design

As outlined in Chapter 1.2, various segmentation techniques were reviewed for detecting dark spots in oil spill images. Among the most commonly utilized approaches, several standout techniques were selected for an in-depth comparison with the proposed semi-empirical model. This includes the Otsu method, Bradley adaptive threshold method, and active contour model (ACM).

The global Otsu method (Otsu, 1979), distinguished by its simple and nonparametric characteristics, has been a prevalent selection for the automatic segmentation of dark spots within grayscale images, notably in the analysis of oil spill detection. It determines an optimal threshold value for a grayscale image separating it into foreground and background by maximizing the between-class variance and minimizing the within-class variance between the designated classes.

While the Otsu method demonstrates efficacy, it exhibits limitations in its application to large SAR imagery. These limitations primarily originate from the suboptimal performance of the Otsu method in handling non-uniform illumination in images, a characteristic resulting from incidence angle variance in SAR imagery. Furthermore, the Otsu method operates under the inherent assumption that both the background and foreground are present within the image. Consequently, even when

oil might not be present in an image, the Otsu method persists in segmentation, relying on differences in brightness values, which may result in the erroneous detection of oil spill candidates.

In response to the challenges posed by non-uniform illumination, the Bradley adaptive threshold method (Bradley and Roth, 2007) has been widely employed as a dark spot segmentation technique as well. Distinct from global threshold methods, the Bradley method computes a local threshold for each pixel, utilizing the mean intensity of the surrounding neighborhood pixels. As a result, this method demonstrates robustness against local variations in intensity, including the brightness value differences arising from variations in SAR incidence angles. Unlike the Otsu method, the Bradley method requires specific tuning parameters, specifically window size, and sensitivity. The window size defines a local region around each pixel, and sensitivity serves as a controlling parameter for the thresholding level within the local window. The careful selection of these parameters is vital because they significantly impact the performance of the algorithm.

In this research, the window size is adaptively adjusted to half the width and height of the SAR image patch size, considering that the patch is properly cropped to encompass the oil spill area. Additionally, the sensitivity parameter, responsible for striking the balance between foreground and background pixels, was meticulously set to 0.3 through a tuning process.

While the Bradley adaptive threshold method is proficient in handling images with non-uniform illumination, it also operates under the assumption that both

background and foreground are present within a defined window. Deformable models such as the ACM are able to segment the foreground area from a noisy background and avoid arbitrary segmentation when no discernible contrast is present. The ACM method, also known as “snakes”, functions as an energy-minimizing spline. It is typically guided by internal forces related to the smoothness of the curve and external forces derived from salient image features such as lines and edges. The goal is to place the initial contour near the desired local minimum, allowing the snakes to iteratively evolve within the image to fit the object boundaries (Kass et al., 1988). The ACM method offers distinct advantages, including the capability to handle images with complex backgrounds and inconsistent illumination. However, it also brings certain challenges to bear, such as sensitivity to the initial positioning of contours, a need for careful adjustment of parameters, and the possibility of incurring high computational costs for processing large or complicated images.

In order to detect dark spot areas from the SAR image patch using the ACM method, several parameters need to be determined. Firstly, the initial contour should be defined. Given that the SAR image patch has been cropped to confine the oil spill area, the initial contour was established along the patch edges, with a thickness of 25 pixels. From this initial contour, the shape is gradually deformed in a manner that minimizes the total energy. In this study, the Chen-Vese active contour method (Chan and Vese, 2001) was utilized, chosen for its efficacy in detecting contours with smooth boundaries, a feature particularly effective for segmenting emulsified oil spills. Through careful parameter tuning, a positive

contraction bias parameter of 0.5 was set, thereby encouraging the inward movement of the contour. The active contour algorithm was configured to terminate when the contour remained unchanged for five consecutive iterations. However, to ensure computational efficiency, a maximum iteration limit of 1500 was imposed.

To summarize, Table 4.1 enumerates all the necessary parameters for different models. Notably, the Otsu method and the semi-empirical model do not require any parameter inputs for execution.

Table 4.1. Parameters required to tune the different methods of detecting dark spots

Method	Required tuning parameters
Otsu Method	(No parameters required)
Bradley Method	<ol style="list-style-type: none"> 1. Window size 2. Sensitivity to determine background and foreground
ACM Method	<ol style="list-style-type: none"> 1. Window size (optional) 2. Initial mask 3. Iteration number 4. Smooth Factor 5. Contraction Bias
Semi-Empirical Method	(No parameters required)

4.2 Performance Evaluation with Other Methods

To assess the performance of the oil spill candidate segmentation model, appropriate evaluation metrics must be established. The confusion matrix offers a comprehensive overview of the relationship between the true condition and the model output. In binary segmentation tasks, four possible outcomes exist: true positive (TP), false positive (FP), true negative (TN), and false negative (FN). TP represents the accurate identification of oil spill candidates by the model. FP pertains to situations where the model incorrectly identifies an oil spill candidate, estimating non-candidate pixels as a false positive prediction. The TN classification occurs when the model correctly recognizes a non-candidate for an oil spill and FN denotes cases where the model mistakenly classifies an oil spill candidate as a non-candidate. Collectively, examining the ratios of these classes offers a comprehensive framework for evaluating the effectiveness and accuracy of the model. In this study, seven metrics are employed, including False Positive Rate (FPR), True Negative Rate (TNR), True Positive Rate (TPR), False Negative Rate (FNR), Precision, Accuracy, and F1 score.

FPR, Eq. (4.1), measures the fraction of background pixels incorrectly identified as foreground pixels. TNR, Eq. (4.2), calculates the proportion of background pixels correctly classified as background pixels. TPR, Eq. (4.3), also known as Recall, quantifies the fraction of foreground pixels correctly identified as foreground pixels. FNR, Eq. (4.4), estimates the proportion of foreground pixels

mistakenly identified as background pixels. Precision, Eq. (4.5) calculates the proportion of true foreground pixels among all identified foreground pixels.

The accuracy, defined as Eq. (4.6), represents the proportion of correctly classified pixels, encompassing both positive and negative instances, out of the total number of pixels in the image. In other words, it quantifies how well the segmentation algorithm has identified both the foreground and background pixels. Serving as a unified metric, it reflects the model's overall ability in the classification. A higher accuracy level indicates the proficient performance of the model in identifying both types of pixels. Nevertheless, accuracy can sometimes be misleading, especially in cases with an imbalanced class distribution, such as when background pixels significantly outnumber or are outnumbered by foreground pixels. In such situations, a high accuracy may merely reflect the successful identification of the majority class, overlooking the potentially inadequate performance of the minority class. Therefore, in the specific context of oil spill detection, where the precise recognition of the minority class (oil) is important, accuracy is not sufficient.

The F1 score, defined as Eq. (4.7), provides a balanced assessment of the model's performance as it represents the harmonic mean of precision and recall. A high F1 score suggests that the segmentation algorithm is proficient in identifying foreground pixels with both high precision and recall.

$$FPR = \frac{FP}{FP + TN} \quad (4.1)$$

$$TNR = \frac{TN}{FP + TN} \quad (4.2)$$

$$TPR (Recall) = \frac{TP}{TP + FN} \quad (4.3)$$

$$FNR = \frac{FN}{TP + FN} \quad (4.4)$$

$$Precision = \frac{TP}{TP + FP} \quad (4.5)$$

$$Accuracy = \frac{TP + TN}{TP + TN + FP + FN} \quad (4.6)$$

$$F1 \text{ score} = \frac{2 \cdot Precision \cdot Recall}{Precision + Recall} \quad (4.7)$$

In Table 4.2, the results for seven distinct metrics are presented for each oil spill candidate detection method. The best-performing result for each metric is highlighted in red, while the second-best result is indicated in blue. For the metrics TPR and FNR, the Otsu method outperformed the others, achieving values of 0.9978 and 0.0022, respectively. In the case of FPR, TNR, and precision, the semi-empirical model yielded the highest values with 0.0464, 0.9536, and 0.8077, respectively. The semi-empirical model also exhibited the best performance in the overall evaluation indicators, specifically accuracy and F1 score, with corresponding values of 0.9487 and 0.7948.

To develop an understanding of the overall performance of each method, the distribution of the F1 scores was visualized using a violin plot, as shown in Fig. 4.1. Within this figure, the red bars on the violins represents the mean F1 score and

revealed that the semi-empirical model achieved the highest performance at approximately 0.7948, followed by the Bradley model at 0.6400, the ACM at 0.5191, and the Otsu model at 0.3315. The median values, with corresponding figures of 0.7027, 0.5662, 0.1801, and 0.1054, also confirm this trend, aligning with the performance pattern observed in the mean.

Table 4.3 presents the statistical metrics of standard deviation and skewness for four different segmentation methods. In the table, the smallest value of standard deviation, representing the most concentrated distribution, is marked in red, and the next smallest value is marked in blue. The proposed semi-empirical model demonstrated the lowest standard deviation at 0.1572, followed by the Bradley method at 0.1972, the Otsu method at 0.2600, and the ACM method, with the highest value of 0.3470. These results indicate that the semi-empirical model performs more consistently across various oil spill instances, whereas the ACM method's effectiveness appears to vary significantly depending on the oil spill cases. The skewness values were also analyzed to assess the asymmetry in the F1 score distribution, where a negative skewness value implies a rightward skew, signifying a direction associated with a higher F1 score. The smallest values were marked in red and the second smallest in blue, similar to the standard deviation. In this regard, the proposed model showed superiority as well, presenting the lowest skewness value of -1.1293. Following this, the Bradley method exhibited a value of -0.7004. The Otsu method displayed a positive skewness value of 0.7307, indicating a leftward skew.

The trends observed in standard deviation and skewness are clearly illustrated in the corresponding violin plots. The ACM method, characterized by the highest standard deviation value, exhibits a bimodal distribution concentrated at both extremes. The Otsu method displays a mild bimodality, whereas the Bradley and semi-empirical methods demonstrate a unimodal distribution that is rightward skewed, emphasizing their consistency in achieving high performance.

For a detailed and qualitative understanding of the performance of each model, Fig. 4.2 presents the segmentation result images for the cases in which each model performed best, while Fig. 4.3 displays the cases where each method showed the worst performance.

The conditions in which the Otsu method achieves the highest performance are when the histogram distribution of oil and background is similar, resulting in a distinct bimodal histogram, as illustrated by item (A2) in Fig. 4.2. However, the presence of exceptional values, such as the strong backscattered signal from ships, can disrupt the bimodality of the histogram. Due to this disruption, most of the region might be incorrectly identified as oil, as consistently demonstrated in the second column of the four images in Fig. 4.3. This effectively explains why the Otsu method has good TPR and FNR values, but suboptimal FPR, TNR, and precision values. When the majority of areas are classified as oil, there is little chance of missing actual oil, yet performance in discriminating non-oil areas accurately tends to be diminished.

The Bradley method showed the best performance when the window size is properly set according to oil spill area size, and when there are no anomalous

pixels present, such as vessels. As well illustrated in Fig. 4.2, item (C3), when the expanse of the oil spill is sufficiently large to encompass the entire window, the moving window fails to discriminate between the oil spill and the background area, as the window is situated within the oil spill region. Additionally, when exceptionally bright pixels appear, the moving window does not correctly distinguish oil spill pixels from the background ocean. Instead, it distinguishes the open ocean from the bright vessel pixels, resulting in a misidentification of vessels as background, and the open ocean as oil spills, as illustrated in Fig. 4.3, item (B3).

The ACM demonstrated the highest performance under conditions where the shape of the oil spill is relatively simple, and the oil spill is densely concentrated rather than dispersed into several sections, as clearly illustrated in Fig. 4.2, item (B4). According to Fig. 4.3, it is apparent that performance is suboptimal when the shape of the oil spill is complex or when the background undergoes abrupt pattern changes. Such conditions may cause the initial contour to either terminate prematurely or converge to an inappropriate area.

Contrary to the previous models, the semi-empirical model appears to be less influenced by factors such as the shape or size of the oil spill, or the presence of vessels. Despite the variety of oil spill cases that exhibit diverse performances in other models, no distinctive dependency was observed with the semi-empirical model. Nevertheless, given the semi-empirical model's potential sensitivity to input variables such as wind speed, a more thorough examination of these aspects needs to be conducted and is to be presented in the following chapter.

Table 4.2. Detailed evaluation of the dark spot detection methods

Metric\Method	Otsu Method	Bradley Method	ACM Method	Semi-Empirical Method
FPR*	0.6186	0.1114	0.3734	0.0464
TNR	0.3814	0.8886	0.6266	0.9536
TPR (Recall)	0.9978	0.9488	0.8305	0.8674
FNR*	0.0022	0.0512	0.1695	0.1326
Precision	0.2349	0.5243	0.5578	0.8077
Accuracy	0.4521	0.8913	0.6591	0.9487
F1 score	0.3315	0.6400	0.5191	0.7948

* The lower values of FPR and FNR indicate better segmentation performance

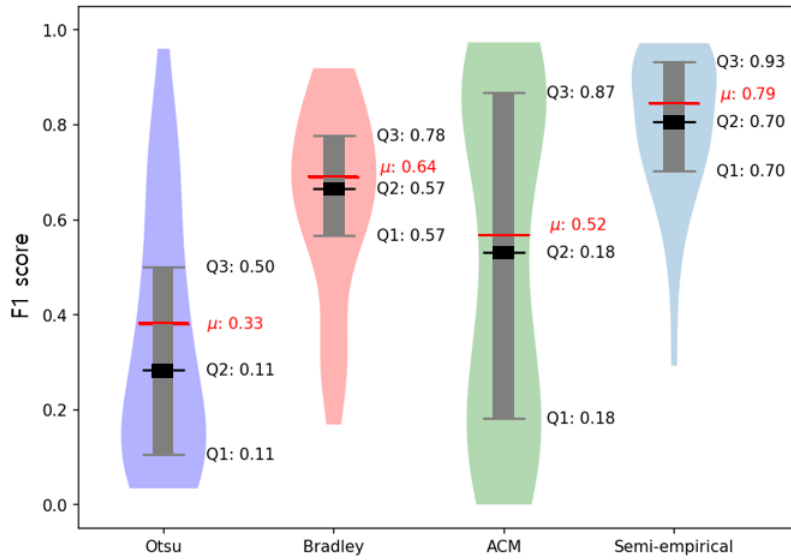


Fig. 4.1. Violin plot illustrating the distribution of the F1 score. Red bars indicate the mean F1 score.

Table 4.3. Standard deviation and skewness for each dark spot detection method

Metric\Method	Otsu Method	Bradley Method	ACM Method	Semi-Empirical Method
Standard deviation	0.2600	0.1972	0.3470	0.1572
Skewness	0.7307	-0.7004	-0.1038	-1.1293

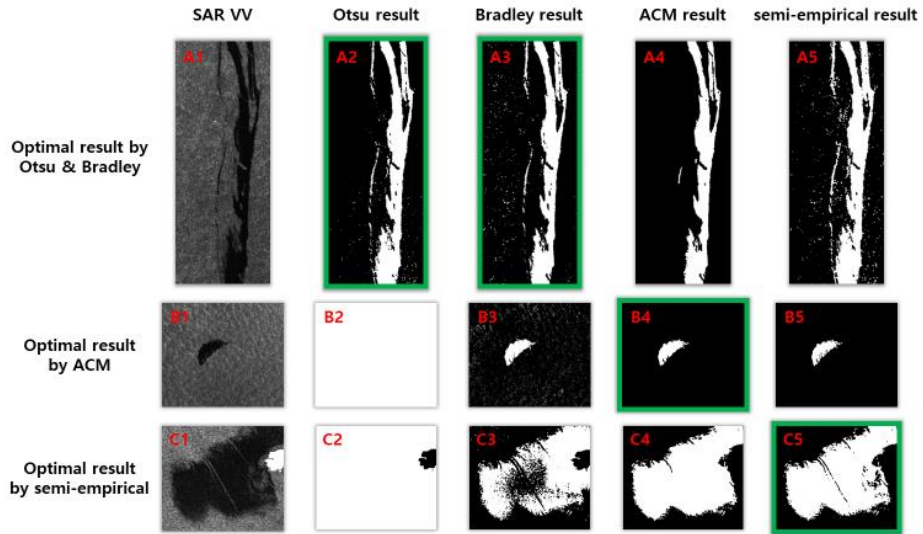


Fig. 4.2. Comparative visualization of the optimal results for various segmentation methods. Each row represents the best-performing case for a given method.

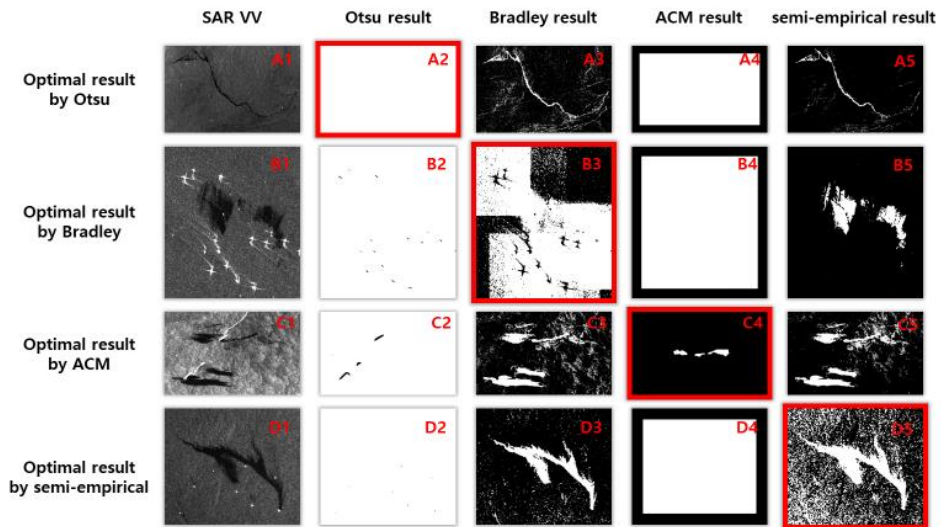


Fig. 4.3. Comparative visualization of the optimal results for various segmentation methods. Each row represents the worst-performing case for a given method.

4.3 Performance Evaluation for Different Wind Conditions and Regions

As the wind wave growth rate elucidates the relationship between the growth of short gravity-capillary waves and wind forcing, ocean wind speed significantly influences the sea state. Consequently, the detectability of oil spills, which is dependent on this sea state, varies with wind levels. In a calm sea state with low wind speeds, microwave backscatter from the surrounding sea surface is too low to distinguish oil from seawater. In contrast, in rough sea conditions, caused by high wind speeds, sufficient microwaves are scattered from the sea surface, yet detection remains difficult due to oil spills being obscured within the wave troughs. In general, a minimum wind speed of 1.5 m/s and a maximum wind speed of 6-10 m/s is recommended for accurate oil spill detection (Hühnerfuss et al., 1996; Akar et al., 2011; Fingas and Brown, 2014). Therefore, this chapter will assess the model's performance in relation to wind speed and delineate the conditions under which the model achieves its best performance.

Fig. 4.4 represents the dependency of each model's performance on wind speed. In models such as Otsu and Bradley, previous qualitative assessments have demonstrated that performance is substantially influenced by factors such as the histogram distribution of the image, the size of oil spills, and the presence of nearby vessels. Contrary to that tendency, a discernible trend correlating performance with wind speed was not observed. Similarly, in the case of the ACM method, which is sensitive to factors like the shape of the oil spill, there is no clear

relationship between wind speed and performance. For the semi-empirical model, as the threshold is determined by wind speed, wind speed exerts a substantial influence on the performance. To identify the impact of wind speed on model performance, the performance of the semi-empirical model was categorized into three bins according to wind speed. The performance within each bin was visualized using violin plots as depicted in Fig. 4.5.

The three bins were categorized as follows: (i) wind speed lower than 2 m/s, (ii) wind speed ranging from 2 to 5 m/s, and (iii) wind speed higher than 5m/s. Within these categories, the model demonstrated the highest performance, with an average F1 score of roughly 0.86, in the 2 to 5 m/sec range. This performance is higher compared to when the wind speed exceeds 5 m/s (average F1 score of about 0.69) or falls below 2 m/s (average F1 score of about 0.65). This outcome can be attributed to the moderate wind speeds which enable sufficient microwave backscattering from the ocean surface.

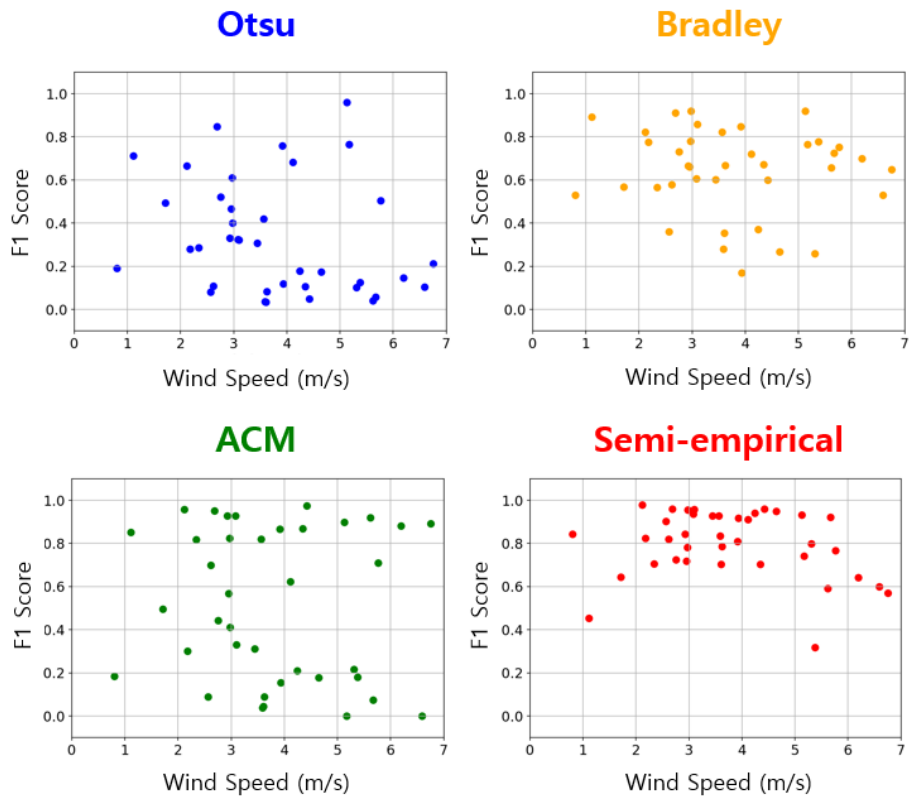


Fig. 4.4. F1 score distribution of each model by wind speed.

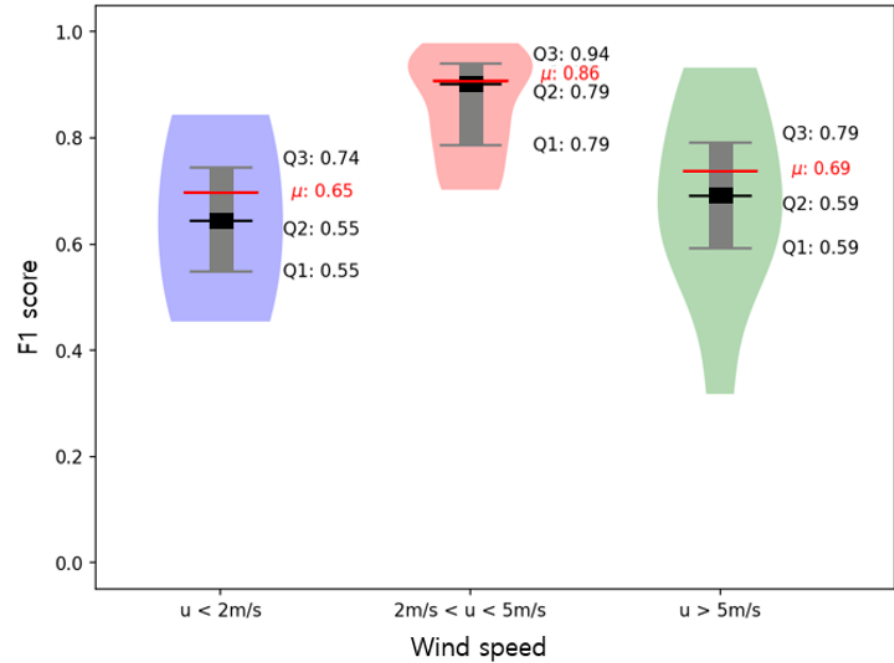
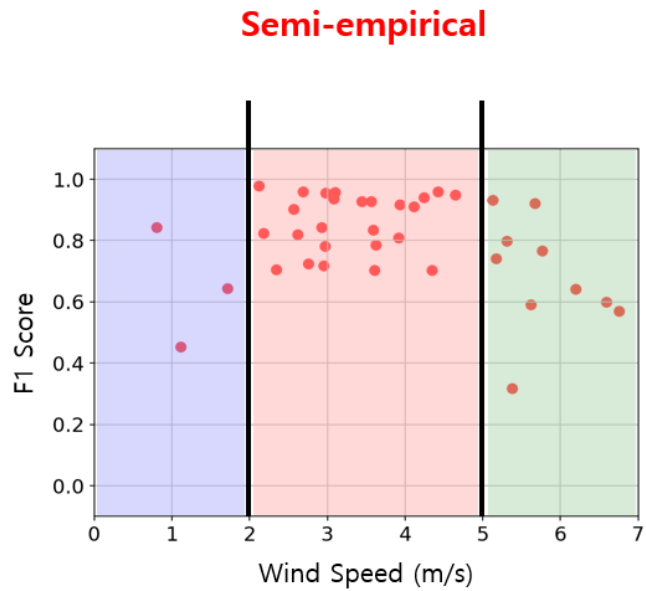


Fig. 4.5. The violin plot of the semi-empirical model F1 score for each wind speed bin.

In previous stages, it was established that the performance of the semi-empirical model is dependent on wind speed, particularly excelling within the range of 2 to 5 m/s. The objective of the current phase is to investigate whether the performance of the proposed model exhibits regional dependency. An examination has been conducted under the assumption that regions with frequent fluctuations in sea state may yield different model performance compared to areas maintaining a stable state. This analysis facilitates a deeper understanding of the regional conditions under which the model demonstrates superior performance. This understanding can contribute to improving model reliability and optimization.

The surface sea state is directly influenced by wind speed, allowing the standard deviation of wind speed to represent the temporal fluctuation of the surface sea state. By utilizing hourly ECMWF ERA5 reanalysis data spanning January to December 2022, the global standard deviation of wind speed was quantified at each grid point. In Fig. 4.6 and Fig. 4.7, the relationship between sea state variability and the F1 score is illustrated in scatter plots. Additionally, the global wind speed standard deviation map is displayed in those figures as well, where Fig. 4.6 shows the points where the model achieved an F1 score higher than 0.9, while Fig. 4.7 emphasizes regions with an F1 score of less than 0.7. An examination of these regions revealed that areas with high temporal ocean surface fluctuation (highlighted in red) tended to demonstrate inconsistent model performance, whereas areas characterized by stable sea states (colored in blue) were associated with more consistent model behavior.

To facilitate a direct comparison, regions where the dark spot segmentation result has F1 score above 0.9 and those below 0.7 were designated with star and triangle-shaped points, respectively. These points were overlaid on the wind speed standard deviation map as depicted in Fig. 4.8 (left). For a more precise analysis, two representative regions were selected: Region A, where the model performance was high, and Region B, where the model performance was lower. A time series analysis of the wind speed for both regions during the year 2022 was undertaken, as shown in Fig. 4.8 (right). In the time series analysis, Region A experienced a relatively stable wind speed throughout the year, corresponding with favorable model performance. Conversely, Region B faced substantial and frequent wind speed fluctuations, which was reflected in the less satisfactory model performance. Therefore, along with the earlier examination of wind speed, this analysis elucidates the specific regional conditions that enhance the model's effectiveness.

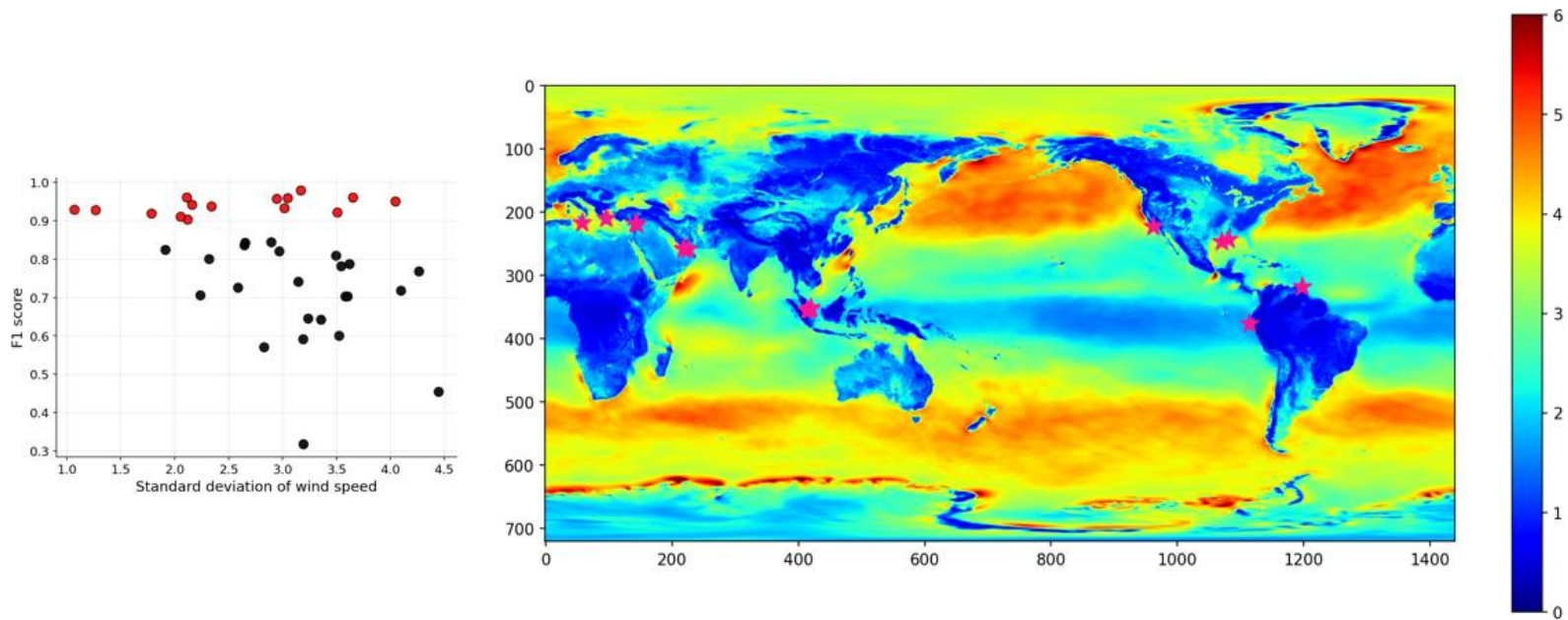


Fig. 4.6. Points where the F1 score is higher than 0.9 are represented on the wind speed standard deviation map.

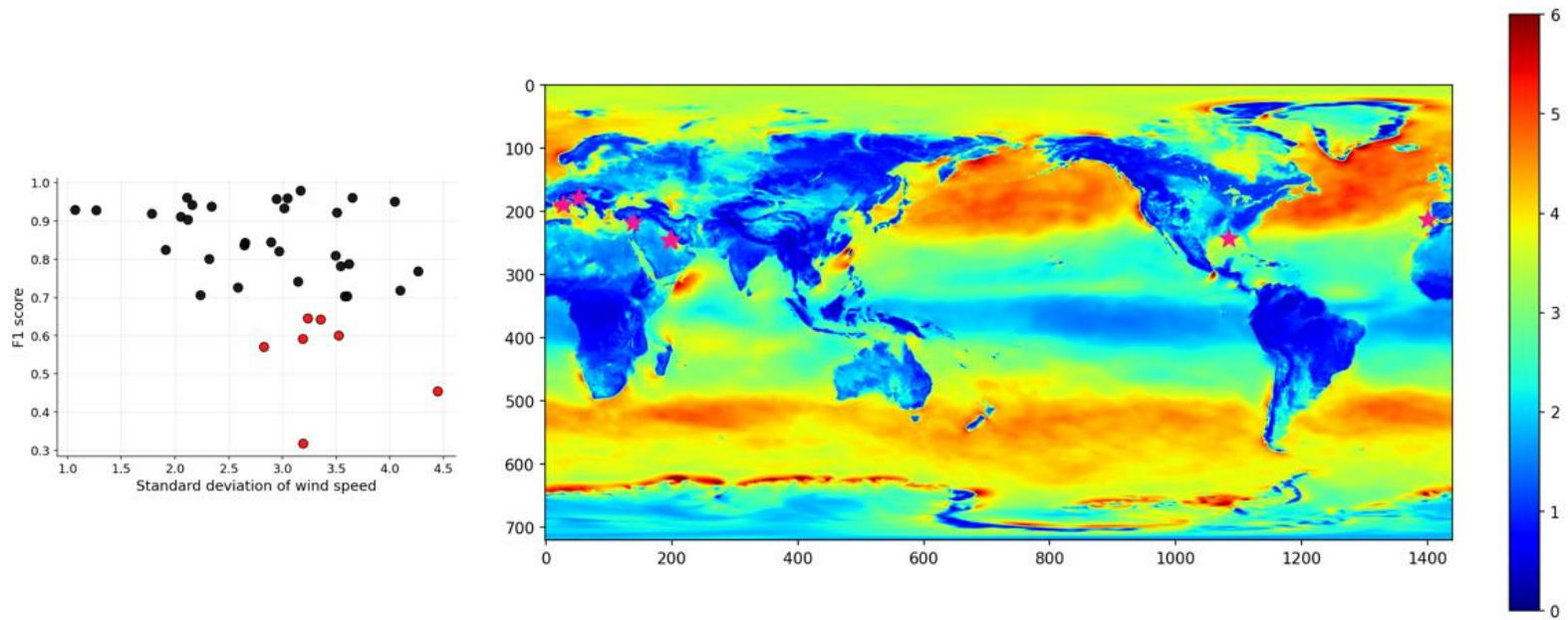


Fig. 4.7. Points where the F1 score is lower than 0.7 are represented on the wind speed standard deviation map.

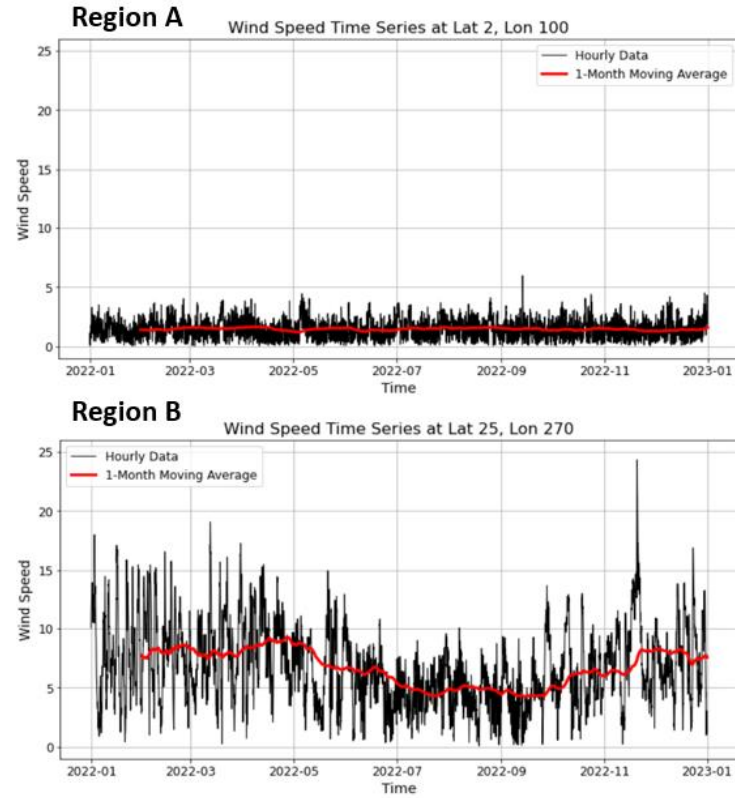
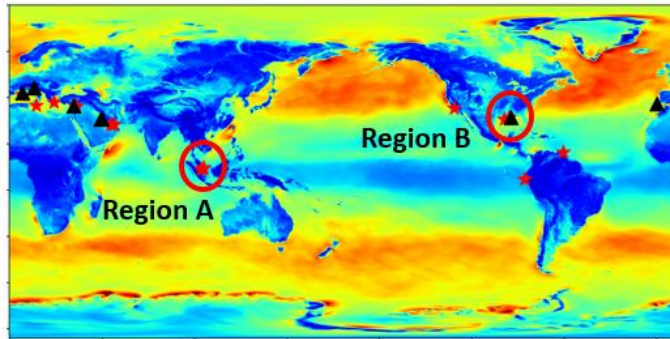


Fig. 4.8. Time-series analysis for wind speed at two regions.

Chapter 5. Application of the Semi-Empirical Model

As the proposed semi-empirical model require the wind field information, the reanalysis data were used for model parameter estimation. However, other sources of wind information such as buoy, scatterometers, and GMF, may also be utilized during the model application stage. Therefore, the proposed model was evaluated using different wind input sources and the two recent oil spill instances in the Gulf of Mexico on January 1, 2023 and March 7, 2023 were used for this evaluation.

To utilize the wind data from buoys, the two-dimensional wind field data, which accordance with the SAR image resolution, need to be extracted. Data were sourced from the National Data Buoy Center (NDBC). Since the precise buoy data corresponding to the exact time and location of the oil spill incidents were unavailable, the two nearest buoys to the spill area, specifically stations 42002 and 42020, were selected. Considering the data recording time interval of the buoy is 10 minutes, two temporally consecutive data points for each oil spill case were selected at the exact times represented in Fig. 5.1, and linear temporal interpolation was first conducted. Subsequently, spatial interpolation based on Euclidean distance was conducted using the data from the two buoys.

The scatterometer data, while more spatially continuous than buoys, exhibit significant temporal gaps. In this study, the advanced scatterometer (ASCAT) data corresponding to the times represented in Fig. 5.1 were utilized. To align with the

resolution of the Sentinel-1 SAR satellite, both linear temporal and spatial interpolation were conducted as well.

The reanalysis data from the ECMWF was applied in a manner consistent with the methodology described in Chapter 3.2.2. Although the reanalysis data provides comprehensive global wind data and relatively dense temporal intervals, it is not good at precisely replicating the state at the exact moment the SAR image was taken. Despite the wind direction ambiguity in the CMOD, it contains precise wind speed at the time point of image capture, making it useful for extracting wind data from the SAR image. Therefore, as a preprocessing step, SAR pixels outside of the interquartile range were smoothed using nearby pixels, and wind data were extracted using CMOD5.N, as described by Eq. 2.7. Fig. 5.1 illustrates the results of applying the semi-empirical model using each of these wind input data sources. Since both the buoy and scatterometer data may not represent the wind state at the exact location and time, the results were less accurate in instances of abrupt wind changes. In this regard, reanalysis data provided better results, and the segmentation result derived from the CMOD demonstrated superior performance.

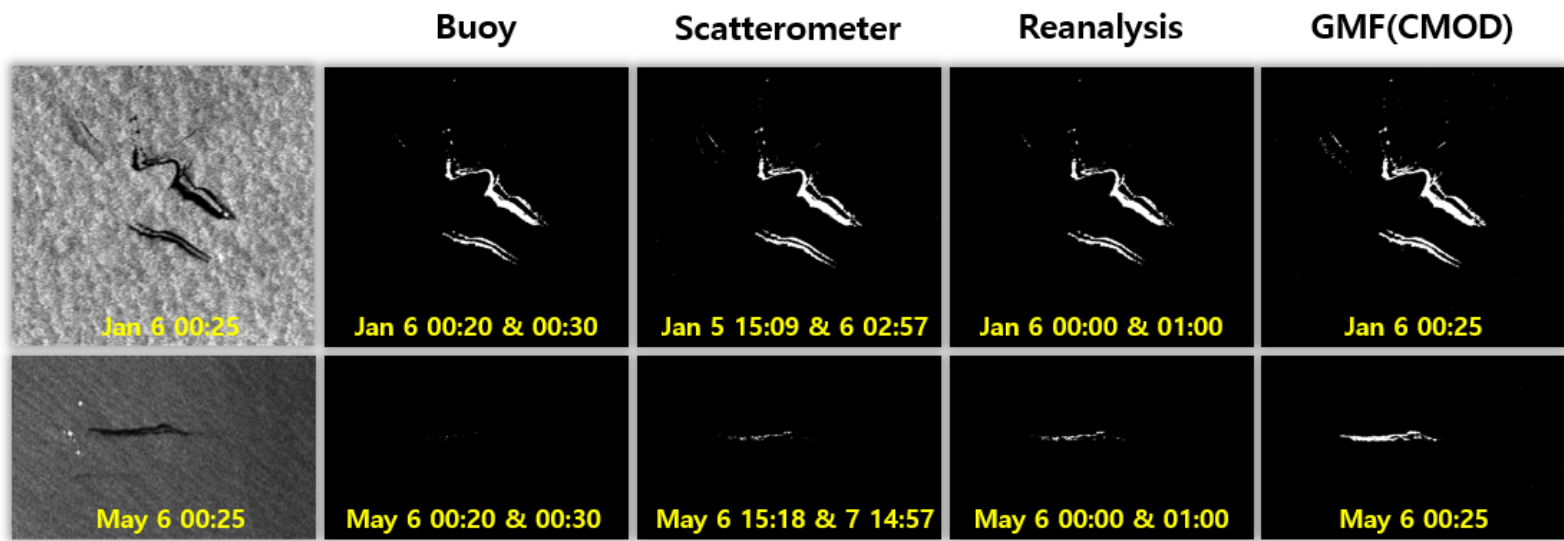


Fig. 5.1. Comparison of results between model input wind dataset.

Chapter 6. Conclusion

In automated oil spill surveillance systems, the dark spot detection step typically demands considerable time and critically influences the overall performance. In this research, a semi-empirical threshold model has been proposed based on the scattering mechanism of the signal on the slick-free and covered sea surface. Utilizing wind speed, relative direction, and incidence angle as inputs, the model was designed to calculate the threshold radar backscatter coefficient value, effectively differentiating potential oil spills.

In the evaluation of the segmentation results by the proposed model, it achieved a superior mean F1 score of 0.7948, in comparison to prevalent methods in dark spot detection such as the Otsu method, Bradley method, and ACM method, with mean F1 scores of 0.3315, 0.6400, and 0.5191, respectively. A more detailed analysis of the F1 score distribution for the evaluation dataset was undertaken to analyze the performance of the proposed model. The bias towards higher F1 scores, indicative of consistently high performance, was visually confirmed through a violin plot. This was further corroborated by quantitative metrics, with the proposed model showing the lowest standard deviation among the four methods, at 0.1572, and the lowest skewness value as well, at -1.1293.

The proposed model distinguishes itself by guaranteeing a notable level of accuracy while employing a straightforward implementation process. This balance between accuracy and simplicity is particularly advantageous in dark spot detection,

where rapid and efficient identification of potential oil spills from the vast ocean is required. By incorporating wind as an input variable and applying SAR ocean imaging physics, the model refines the identification of oil spill candidates, effectively eliminating low wind areas and common false positives in oil spill detection. Furthermore, a distinguishing feature of the proposed model is its capacity to compute the threshold radar backscatter coefficient at a pixel level. Contrasting with conventional approaches that function on a patch level, necessitating various window sizes and iterative operations to detect oil spills of different sizes, this model detects oil spill candidates in a SAR image in a single step. This characteristic not only streamlines the detection process but also enhances the model's adaptability and efficiency, making it a robust tool for handling a wide range of oil spill conditions.

While the proposed model demonstrates significant advantages in detecting oil spill candidates, it is important to recognize the underlying dependencies that characterize its performance. The model's performance was found to be dependent on wind speed and regional characteristics. Optimal results can be achieved within a moderate wind speed range of 2 to 5 m/sec, especially in regions that exhibit minimal temporal wind speed variance. Specifically, the accuracy of the model was significantly influenced by how precisely the wind field information mirrored the actual wind state at the exact time the SAR image was captured.

In conclusion, the application of this model to oil spill monitoring systems could enhance operational efficiency, enabling more targeted analysis of vast ocean data. As demonstrated in previous work (Shaban et al., 2021), this model offers

practical applications, such as aiding in the construction of balanced deep-learning datasets by selectively choosing patches containing dark spots. Moreover, the physically-grounded nature of this model creates opportunities for future research in advanced oil spill detection, including distinguishing oil types or estimating slick thickness.

Bibliography

- Akar, S., Süzen, M. L., and Kaymakci, N. (2011). Detection and object-based classification of offshore oil slicks using ENVISAT-ASAR images. *Environmental Monitoring and Assessment*, 183, 409–423.
- Alpers, W., Holt, B., and Zeng, K. (2017). Oil spill detection by imaging radars: Challenges and pitfalls. *Remote Sensing of Environment*, 201, 133–147.
- Alpers, W., and Hühnerfuss, H. (1988). Radar signatures of oil films floating on the sea surface and the Marangoni effect. *Journal of Geophysical Research: Oceans*, 93(C4), 3642–3648.
- Alpers, W., and Hühnerfuss, H. (1989). The damping of ocean waves by surface films: A new look at an old problem. *Journal of Geophysical Research: Oceans*, 94(C5), 6251–6265.
- Bianchi, F. M., Espeseth, M. M., and Borch, N. (2020). Large-scale detection and categorization of oil spills from SAR images with deep learning. *Remote Sensing*, 12(14), 2260.
- Bradley, D., and Roth, G. (2007). Adaptive thresholding using the integral image. *Journal of Graphics Tools*, 13(21).
- Brekke, C., and Solberg, A. H. S. (2005). Oil spill detection by satellite remote sensing. *Remote Sensing of Environment*, 95(1), 1–13.
- Callaghan, I. C., Gould, C. M., Hamilton, R. J., and Neustadter, E. L. (1983). The relationship between the dilatational rheology and crude oil foam stability. I. Preliminary studies. *Colloids and Surfaces*, 8(1), 17–28.
- Chan, T. F., and Vese, L. A. (2001). Active contours without edges. *IEEE Transactions on Image Processing*, 10(2), 266–277.
- Chen, F., Zhou, H., Grecos, C., and Ren, P. (2018). Segmenting oil spills from blurry images based on alternating direction method of multipliers. *IEEE Journal of Selected Topics in Applied Earth Observations and Remote Sensing*, 11(6), 1858–1873.
- Chen, Y., and Wang, Z. (2022). Marine oil spill detection from SAR images based on attention U-Net model using polarimetric and wind speed information.

International Journal of Environmental Research and Public Health, 19(19), 12325.

- Del Frate, F., Petrocchi, A., Lichtenegger, J., and Calabresi, G. (2000). Neural networks for oil spill detection using ERS-SAR data. *IEEE Transactions on Geoscience and Remote Sensing*, 38(5), 2282–2287.
- Elfouhaily, T., Chapron, B., Katsaros, K., and Vandemark, D. (1997). A unified directional spectrum for long and short wind-driven waves. *Journal of Geophysical Research: Oceans*, 102(C7), 15781–15796.
- Espedal, H. A., and Wahl, T. (1999). Satellite SAR oil spill detection using wind history information. *International Journal of Remote Sensing*, 20(1), 49–65.
- Fingas, M., and Brown, C. (2014). Review of oil spill remote sensing. *Marine Pollution Bulletin*, 83(1), 9–23.
- Franceschetti, G., Fellow, L., Iodice, A., Riccio, D., Member, S., Ruello, G., Member, S., and Siviero, R. (2002). SAR raw signal simulation of oil slicks in ocean environments. *IEEE Transactions on Geoscience and Remote Sensing*, 40(9), 1935–1949.
- Gade, M., and Alpers, W. (1999). Using ERS-2 SAR images for routine observation of marine pollution in European coastal waters. *The Science of the Total Environment*, 237(238), 441–448.
- Gade, M., Alpers, W., Hühnerfuss, H., Wismann, V. R., and Lange, P. A. (1998). On the reduction of the radar backscatter by oceanic surface films: Scatterometer measurements and their theoretical interpretation. *Remote Sensing of Environment*, 66(1), 52–70.
- Hersbach, H. (2003). *CMOD5 An improved geophysical model function for ERS C-band scatterometry*. ECMWF. <http://www.ecmwf.int/publications/>
- Hersbach, H. (2008). *CMOD5. N: A C-band geophysical model function for equivalent neutral wind*. ECMWF. <http://www.ecmwf.int/publications/>
- Huang, B., Li, H., and Huang, X. (2005). A level set method for oil slick segmentation in SAR images. *International Journal of Remote Sensing*, 26(6), 1145–1156.

- Hühnerfuss, H., Alpers, W., Dannhauer, H., Gade, M., Lange, P. A., Neumann, V., and Wismann, V. (1996). Natural and man-made sea slicks in the North Sea investigated by a helicopter-borne 5-frequency radar scatterometer. *International Journal of Remote Sensing*, 17(8), 1567–1582.
- Hwang, P. A., Zhang, B., Toporkov, J. V, and Perrie, W. (2010). Comparison of composite Bragg theory and quad-polarization radar backscatter from RADARSAT-2: With applications to wave breaking and high wind retrieval. *Journal of Geophysical Research: Oceans*, 115(C8).
- Isoguchi, O., and Shimada, M. (2009). An L-band ocean geophysical model function derived from PALSAR. *IEEE Transactions on Geoscience and Remote Sensing*, 47(7), 1925–1936.
- Karantzalos, K., and Argialas, D. (2008). Automatic detection and tracking of oil spills in SAR imagery with level set segmentation. *International Journal of Remote Sensing*, 29(21), 6281–6296.
- Karathanassi, V., Topouzelis, K., Pavlakis, P., and Rokos, D. (2006). An object-oriented methodology to detect oil spills. *International Journal of Remote Sensing*, 27(23), 5235–5251.
- Kass, M., Witkin, A., and Terzopoulos, D. (1988). Snakes: Active contour models. *International Journal of Computer Vision*, 1(4), 321–331.
- Keramitsoglou, I., Cartalis, C., and Kiranoudis, C. T. (2006). Automatic identification of oil spills on satellite images. *Environmental Modelling and Software*, 21(5), 640–652.
- Konik, M., and Bradtke, K. (2016). Object-oriented approach to oil spill detection using ENVISAT ASAR images. *ISPRS Journal of Photogrammetry and Remote Sensing*, 118, 37–52.
- Krestenitis, M., Orfanidis, G., Ioannidis, K., Avgerinakis, K., Vrochidis, S., and Kompatsiaris, I. (2019). Oil spill identification from satellite images using deep neural networks. *Remote Sensing*, 11(15), 1762.
- Liu, P., Zhao, C., Li, X., He, M., and Pichel, W. (2010). Identification of ocean oil spills in SAR imagery based on fuzzy logic algorithm. *International Journal of Remote Sensing*, 31(17), 4819–4833.

- Li, X. M., and Lehner, S. (2013). Algorithm for sea surface wind retrieval from TerraSAR-X and TanDEM-X data. *IEEE Transactions on Geoscience and Remote Sensing*, 52(5), 2928–2939.
- Marghany, M. (2014). Utilization of a genetic algorithm for the automatic detection of oil spill from RADARSAT-2 SAR satellite data. *Marine Pollution Bulletin*, 89(1–2), 20–29.
- Mdakane, L. W., and Kleynhans, W. (2017). An image-segmentation-based framework to detect oil slicks from moving vessels in the Southern African oceans using SAR imagery. *IEEE Journal of Selected Topics in Applied Earth Observations and Remote Sensing*, 10(6), 2810–2818.
- Mihoub, Z., and Hassini, A. (2014). Monitoring and identification of marine oil spills using advanced synthetic aperture radar images. *Optica Applicata*, 44(3), 433–449.
- Mitsuyasu, H., and Honda, T. (1982). Wind-induced growth of water waves. *Journal of Fluid Mechanics*, 123, 425–442.
- Mitsuyasu, H., and Honda, T. (1986). The Effects of Surfactant on Certain Air—Sea Interaction Phenomena. *Wave Dynamics and Radio Probing of the Ocean Surface*, 95–115.
- Nirchio, F., and Venafrà, S. (2013). XMOD2—An improved geophysical model function to retrieve sea surface wind fields from cosmo-sky med X-band data. *European Journal of Remote Sensing*, 46(1), 583–595.
- Otsu, N. (1979). A threshold selection method from gray-level histograms. *IEEE Transactions on Systems, Man, and Cybernetics*, 9(1), 62–66.
- Padmasini, N., Umamaheswari, R., and Sikkandar, M. Y. (2018). State-of-the-Art of Level-Set Methods in Segmentation and Registration of Spectral Domain Optical Coherence Tomographic Retinal Images. *Soft Computing Based Medical Image Analysis*, 163–181.
- Phillips, O. M. (1977). *The dynamics of the upper ocean*. Cambridge University Press.
- Plant, W. J. (1982). A relationship between wind stress and wave slope. *Journal of Geophysical Research: Oceans*, 87(C3), 1961–1967.

- Quilfen, Y., Chapron, B., Elfouhaily, T., Katsaros, K., and Tournadre, J. (1998). Observation of tropical cyclones by high-resolution scatterometry. *Journal of Geophysical Research: Oceans*, 103(C4), 7767–7786.
- Romeiser, R., Alpers, W., and Wismann, V. (1997). An improved composite surface model for the radar backscattering cross section of the ocean surface 1. Theory of the model and optimization/validation by scatterometer data. *Journal of Geophysical Research: Oceans*, 102(C11), 25237–25250.
- Salvatori, L., Bouchaib, S., Frate, F. Del, Lichtenegger, J., and Smara, Y. (2003). Estimating the wind vector from radar SAR images when applied to the detection of oil spill pollution. *International Symposium on GIS and Computer Cartography for Coastal Zone Management*.
- Shaban, M., Salim, R., Khalifeh, H. A., Khelifi, A., Shalaby, A., El-Mashad, S., Mahmoud, A., Ghazal, M., and El-Baz, A. (2021). A deep-learning framework for the detection of oil spills from SAR data. *Sensors*, 21(7).
- Shu, Y., Li, J., Yousif, H., and Gomes, G. (2010). Dark-spot detection from SAR intensity imagery with spatial density thresholding for oil-spill monitoring. *Remote Sensing of Environment*, 114(9), 2026–2035.
- Singha, S., Bellerby, T. J., and Trieschmann, O. (2013). Satellite oil spill detection using artificial neural networks. *IEEE Journal of Selected Topics in Applied Earth Observations and Remote Sensing*, 6(6), 2355–2363.
- Singha, S., Ressel, R., Velotto, D., and Lehner, S. (2016). A Combination of Traditional and Polarimetric Features for Oil Spill Detection Using TerraSAR-X. *IEEE Journal of Selected Topics in Applied Earth Observations and Remote Sensing*, 9(11), 4979–4990.
- Solberg, A. H. S., Brekke, C., and Husøy, P. O. (2007). Oil spill detection in Radarsat and Envisat SAR images. *IEEE Transactions on Geoscience and Remote Sensing*, 45(3), 746–754.
- Solberg, A. H. S., Storvik, G., Solberg, R., and Volden, E. (1999). Automatic detection of oil spills in ERS SAR images. *IEEE Transactions on Geoscience and Remote Sensing*, 37(4), 1916–1924.

- Stoffelen, A., and Anderson, D. (1997). Scatterometer data interpretation: Estimation and validation of the transfer function CMOD4. *Journal of Geophysical Research: Oceans*, 102(C3), 5767–5780.
- Topouzelis, K., Karathanassi, V., Pavlakis, P., and Rokos, D. (2007). Detection and discrimination between oil spills and look-alike phenomena through neural networks. *ISPRS Journal of Photogrammetry and Remote Sensing*, 62(4), 264–270.
- Topouzelis, K., and Psyllos, A. (2012). Oil spill feature selection and classification using decision tree forest on SAR image data. *ISPRS Journal of Photogrammetry and Remote Sensing*, 68(1), 135–143.
- Valenzuela, G. R. (1978). Theories for the interaction of electromagnetic and oceanic waves—A review. *Boundary-Layer Meteorology*, 13(1–4), 61–85.
- Wismann, V., Gade, M., Alpers, W., and Hühnerfuss, H. (1993). Radar signatures of mineral oil spills measured by an airborne multi-frequency multi-polarization microwave scatterometer. *Proceedings of the Conference on Oceans '93*, 348–353.
- Wright, J. W. (1968). A new model for sea clutter. *IEEE Transactions on Antennas and Propagation*, 16(2), 217–223.
- Xia, G.-S., Liu, G., Yang, W., and Zhang, L. (2015). Meaningful object segmentation from SAR images via a multiscale nonlocal active contour model. *IEEE Transactions on Geoscience and Remote Sensing*, 54(3), 1860–1873.
- Xu, L., Li, J., and Brenning, A. (2014). A comparative study of different classification techniques for marine oil spill identification using RADARSAT-1 imagery. *Remote Sensing of Environment*, 141, 14–23.
- Yelland, M., and Taylor, P. K. (1996). Wind stress measurements from the open ocean. *Journal of Physical Oceanography*, 26(4), 541–558.
- Yu, F., Sun, W., Li, J., Zhao, Y., Zhang, Y., and Chen, G. (2017). An improved Otsu method for oil spill detection from SAR images. *Oceanologia*, 59(3), 311–317.

Zeng, K., and Wang, Y. (2020). A deep convolutional neural network for oil spill detection from spaceborne SAR images. *Remote Sensing*, 12(6).

Abstract in Korean

SAR 위성을 활용한 자동 유류오염 모니터링 시스템에서 유류오염 후보를 탐지하는 과정인 dark spot detection 단계는, 시스템의 첫 번째 단계로서 일반적으로 가장 많은 시간이 소요되고, 최종 탐지 성능에 결정적인 영향을 미친다. 넓은 해상 영역을 효과적으로 감시하기 위해서는, 이와 같이 초기 단계에서 유류오염 후보를 정확하고 효율적으로 식별할 필요성이 강조된다. 본 논문에서는 전자기파와 유류막으로 덮인 해양 표면 간의 상호작용에 대한 광범위한 분석과 유류오염 위성 관측값을 기반으로 준경험적 모델을 제시하였다. 제안된 모델은 풍속, 상대 풍향, 입사각을 독립변수로 가지며 바다와 유류오염 후보를 효과적으로 구분하는 레이더 후방산란 계수의 임계값을 산출한다. 모델의 매개변수를 결정하기 위해, Sentinel-1 위성에서 대량의 유류오염 관측 데이터를 수집하였고, 이에 해당하는 바람장 데이터를 ECMWF ERA5 재분석 데이터로부터 추출하여 사용하였다.

본 연구에서 제안한 모델의 segmentation 성능 평가 결과, 평균 F1 점수는 0.7948 로 나타났으며, 기존의 대표적인 접근방법인 Otsu, Bradley, active contour model의 성능이 각각 0.3315, 0.6400, 0.5191 인 것과 비교하여 우수한 탐지 성능을 보였다. 해당 모델은 물리적 특성을 고려한 직관적인 알고리즘과 높은 segmentation 정확도로, 특히 효율성이 강조되는 실시간 유류오염 모니터링에 매우 적합하다. 또한 제안된 모델은 픽셀 단계의 임계값 계산이 가능하여, 다른 patch 단위로 동작하는 탐지 모델들과 달리, 다양한 크기의 유류오염을 탐지하기 위해 여러 크기의 윈도우를 반복적으로 사용하여 탐지할 필요가 없다. 해당 모델은 해상 부이, 산란계와 같은 다양한

바람장 정보를 입력값으로 사용할 수 있으나, 모델의 성능은 해당 데이터의 정확도에 크게 의존하며, 특히 SAR 이미지 취득 시점의 바람 상태를 얼마나 정확히 반영하는지에 따라 달라진다는 특징을 가진다.

결론적으로, 본 논문에서는 유류오염이 없는 바다 표면과 있는 표면에서의 레이더 후방산란 계수의 변화를 세밀하게 분석하여, 유류오염 모니터링 시스템의 효율성을 강화할 수 있는 준경험적 유류오염 후보 추출 임계값 모델을 개발하였다. 제안된 모델은 모니터링 시스템의 성능을 향상시킬 수 있을 뿐만 아니라, dark spot이 있는 patch를 선별하여 균형잡힌 딥러닝 데이터셋을 생성하는 데에도 활용될 수 있다. 또한, 본 모델은 유류오염과 해양의 물리적 특성에 근거하므로, 유종 식별 또는 유류 두께추정과 같은 후속 연구의 가능성을 제시한다.

주요어 : 합성개구레이더, 유류오염, 기름유출, 마이크로파 후방산란, 반경험적 모델, 의미론적 분할